



Assessment of dynamical models for transitioning from the Circular Restricted Three-Body Problem to an ephemeris model with applications

Beom Park¹ · Kathleen C. Howell¹

Received: 26 June 2023 / Revised: 5 December 2023 / Accepted: 29 December 2023 /

Published online: 7 February 2024

© The Author(s), under exclusive licence to Springer Nature B.V. 2024

Abstract

While the Circular Restricted Three-Body Problem (CR3BP) provides useful structures for various applications, transitioning the solutions from the CR3BP to a higher-fidelity ephemeris model while maintaining specific characteristics remains non-trivial. An analytical approach is leveraged to provide additional insight on the perturbations that are present in an ephemeris model. For the Earth–Moon CR3BP, pulsation of the Earth–Moon distance and solar gravity are identified as key components contributing to the additional accelerations, where patterns are illustrated through simplified mathematical relationships and graphics. Utilizing these findings, capabilities and limitations of two intermediate models, the Elliptic Restricted Three-Body Problem and the Bi-Circular Restricted Four-Body Problem, are assessed within the context of transitioning from the CR3BP to a realistic ephemeris model. A sample transition process for Earth–Moon L2 halo orbits is provided, leveraging the insight from the proposed analytical approach.

Keywords Ephemeris transition · CR3BP · ER3BP · BCR4BP

1 Introduction

The dynamical structures that exist in the Earth–Moon Circular Restricted Three-Body Problem (CR3BP) are integral to trajectory design for multiple types of missions in cislunar space. Libration points and the associated periodic or quasi-periodic orbits may serve as science orbits to meet various objectives. For example, the Acceleration, Reconnection, Turbulence and Electrodynamics of the Moon’s Interaction with the Sun (ARTEMIS) spacecraft successfully leveraged Lissajous orbits in the vicinity of both L_1 and L_2 for multiple heliophysics and planetary objectives in 2010 (Angelopoulos 2011). The science orbit for JAXA’s EQUi-

✉ Beom Park
park1103@purdue.edu

Kathleen C. Howell
howell@purdue.edu

¹ School of Aeronautics and Astronautics, Purdue University, 701 W. Stadium Avenue, West Lafayette, IN 47907, USA

libriUm Lunar-Earth point 6U Spacecraft (EQUULEUS) includes an L₂ quasi-halo orbit to demonstrate the trajectory control capabilities for a CubeSat (Oguri et al. 2020). The Gateway mission, as proposed by NASA, is also expected to deliver a hub-like facility into an L₂ 9:2 Near Rectilinear Halo Orbit (NRHO), leveraging the stability and eclipse properties of the orbit (Crusan et al. 2018).

While the CR3BP offers diverse structures suited for a variety of trajectories and enables mission design in a simplified dynamical environment, a higher-fidelity model, that is critical for flight, inevitably introduces additional forces. In the cislunar space environment, assuming a point-mass model for the celestial bodies, some of the most impactful forces originate from the non-uniform pulsation of the Earth–Moon system (“pulsation”) and any additional gravitational bodies, mainly the Sun. Depending on the region, these forces may be non-negligible and can impact the solution significantly. Thus, transitioning the CR3BP dynamical structures into their counterparts or analogs within a higher-fidelity model can be a nontrivial process. Numerical procedures that leverage differential correctors are typically employed, often paired with optimizers to enforce desired characteristics (Oguri et al. 2020) or to minimize the deviation from the original solution designed within the CR3BP (Dei Tos and Topputo 2017b; Olikara 2016).

Given an orbit or trajectory that is constructed in the CR3BP, transitioning such a solution to a higher-fidelity dynamical model without leveraging any intermediate models is termed here as a “direct” approach. As the additional forces are unmodeled in the CR3BP, the direct approach relies on the specifics of the numerical schemes to produce successful results. Multiple patchpoints, rather than a single patchpoint, are frequently employed, where the original CR3BP solution is discretized and transformed to an initial guess within a higher-fidelity model. The transformation procedure typically involves a rotation and dimensionalization process, where the instantaneous distance between the gravitational bodies is retrieved from the ephemerides and aids in an appropriate scaling process (Ocampo 2003; Oguri et al. 2020). The results of the transition also depend on other components of the numerical schemes including the number of patchpoints, propagation direction, and the baseline epoch for the transition (Davis et al. 2017; Williams et al. 2017). The direct approach offers a simple yet versatile transition method that produces desired results for many regions throughout cislunar space. However, due to the innate limitations of the CR3BP to incorporate some of the additional forces into the solution, the direct approach may require more “trial-and-error” steps with different numerical formulations. This endeavor, for example, includes searching for a favorable baseline epoch when the desired characteristics are better preserved; as the CR3BP is a time-independent model, it provides only limited information regarding the epoch. Furthermore, previous authors (Davis et al. 2017; Boudad et al. 2022) note that some periodic orbits in the Earth–Moon L₂ halo family, e.g., those close to the 3:1 synodic resonance, do not maintain their geometry within a higher-fidelity model, which serves as a sample case where the direct transition is particularly challenging.

One alternative to the direct approach is a strategy to explicitly leverage intermediate models that potentially bridge the gap between the CR3BP and a higher-fidelity ephemeris model by incorporating some time-dependent characteristics. Such a strategy is particularly important if a key requirement of an ephemeris result is expected to closely retain the geometry or other characteristics designed in a lower-fidelity model. For example, Gómez et al. (2002) identify five basic frequencies in the Earth–Moon system to construct an intermediate model and produce dynamical substitutes for collinear libration points. Similar techniques are employed to analyze the motion of spacecraft near the triangular libration points (Hou and Liu 2010) and on quasi-halo orbits (Lian et al. 2013; Dei Tos and Topputo 2017b). While leveraging multiple frequencies aids in constructing an intermediate model that closely approximates

a higher-fidelity ephemeris model in general, the complexity of such a model may render it impractical for applications. For example, periodic orbits in the CR3BP potentially evolve into multi-dimensional quasi-periodic orbits, where the exact computation of such structures becomes intractable with more frequencies added to the model (McCarthy 2022).

Rather than incorporating multiple frequencies at once, *periodically* perturbed systems are constructed that are governed by one frequency, introducing an additional force in an ideal form. These models include, but are not limited to, the Elliptic Restricted Three-Body Problem (ER3BP), the Bi-Circular Restricted Four-Body Problem (BCR4BP), the Quasi-Bi-Circular Four-Body Problem (QBCP), and the Hill-Restricted Four-Body Problem (HR4BP). Periodic orbits in the CR3BP generally evolve into periodic orbits or quasi-periodic orbits (Jorba and Villanueva 1997) in these models, enabling a systematic assessment and characterization of the impact from the ideal additional perturbing forces (Boudad et al. 2020; Ferrari and Lavagna 2018). Moreover, the unique structures within these models may bridge the gap that exists between the CR3BP and a higher-fidelity ephemeris model and serve as effective, evolving initial guesses for transition, particularly when maintaining the characteristics of the lower-fidelity solution is critical. Multiple authors (Boudad et al. 2022; Dei Tos and Topputo 2017a; Jorba-Cusco et al. 2018; Sanaga and Howell 2023) discuss the potential benefits of leveraging these one-frequency intermediate models for smoother transition from the CR3BP to a higher-fidelity ephemeris model.

A challenge still exists, however, in selecting a suitable one-frequency intermediate model for the transition process. As these models introduce the additional forces into the CR3BP only in ideal forms, they are not guaranteed to be “more accurate” for a given epoch or system configuration. Moreover, as they selectively introduce only one frequency, perturbations associated with other frequencies are not addressed. For instance, the ER3BP, commonly associated with the sidereal frequency of the Earth–Moon system, has limitations in modeling realistic perturbations primarily associated with the synodic frequency, such as solar gravity. Similarly, the BCR4BP and QBCP are governed by the synodic frequency and, thus, incorporating information related to the sidereal frequency poses challenges for these models. Consequently, the intermediate models’ ability to evolve the solution to the full ephemeris representation is expected to rely on several factors, including the epoch and spacecraft state, and the “best” intermediate model may vary. Achieving an efficient transition process requires a deeper understanding of these factors, as incorporating intermediate models with a single frequency increases complexity compared to a direct transition from the CR3BP.

The goal of the current effort is an assessment of various dynamical models to provide beneficial insight concerning the transitioning process from the CR3BP to a higher-fidelity ephemeris model. The main focus is not on providing an accurate description of the higher-fidelity ephemeris model itself, but rather on analyzing the key features of the higher-fidelity model. These features are then utilized to select appropriate one-frequency intermediate models that assist the numerical transition process to deliver the desired characteristics. In line with this goal, the current work aims to address the following issues: (1) identification of the impact of the additional forces on an arc within a higher-fidelity model from an analytical approach, (2) description of the additional forces with intuitive patterns leveraging frequency information, (3) evaluation of sample one-frequency intermediate models, the ER3BP and the BCR4BP, to represent the respective forces in a more global sense within cis-lunar space, and (4) demonstration of the procedure to incorporate these models for a successful ephemeris transition process for a challenging application. The ER3BP and BCR4BP are selected as the intermediate models due to their simplicity and frequent use in previous research.

The dynamical models are initially defined in Sect. 2, where the Equations Of Motion (EOMs) are cast within a common coordinate frame to facilitate analysis. Then, the EOMs are rearranged leveraging a unique isochronous relationship to yield patterns and dominant frequencies concerning the effects of the additional forces within an ephemeris model in Sect. 3. The capabilities and limitations of the ER3BP and BCR4BP in describing the respective additional forces are noted in Sect. 4. The applicability of the ER3BP and the BCR4BP within the Earth–Moon system is demonstrated by introducing a sample transition process from a lower- to higher-fidelity model in Sect. 5. Finally, concluding remarks are provided in Sect. 6.

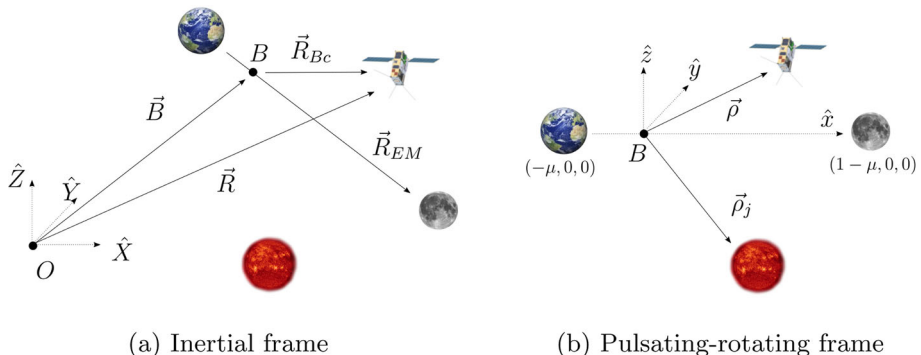
2 Dynamical models

In the current investigation, the focus involves four dynamical models: CR3BP, ER3BP, BCR4BP, and the Higher-Fidelity Ephemeris Model (HFEM). The differential equations governing the behavior in the HFEM are usually represented in an inertial frame, e.g., J2000 frame, whereas the restricted multi-body problems are typically cast within a rotating frame where the primaries, Earth and the Moon, are located at fixed positions. To cope with this discrepancy, Gómez et al. (2002) introduce a pulsating–rotating frame where the HFEM is now represented in a similar form as compared to the CR3BP, but under realistic perturbations from the additional forces, a formulation that is well-suited for the current work. The definition of the pulsating–rotating frame is reviewed, followed by a common form of the EOMs for the various models that are under investigation within this frame. The assumptions and the analytical expressions for the coefficients in the EOMs for each model are provided. Finally, the isochronous correspondence between the models, necessary to accommodate the different independent variables in the models, is also detailed.

2.1 Inertial frame and pulsating–rotating frame

The relationship between the inertial frame and the pulsating–rotating frame is first constructed. Without losing generality, the spacecraft (s/c) is under the gravitational influence of Earth and the Moon, i.e., the primaries, and the additional bodies that are incorporated in the model. By assumption, a point-mass model is utilized for the gravitational bodies. Subscripts E , M , and j denote Earth, the Moon, and the additional bodies, respectively, where j is an element of the set of additional bodies, \mathcal{A} . For example, if the Sun is included as the only additional body, $\mathcal{A} = \{\text{Sun}\}$. An inertial frame is illustrated in Fig. 1a, where the origin O is located at an inertially fixed point, which may be defined differently depending on the models. Unit vectors $\hat{X} - \hat{Y} - \hat{Z}$ define the mutually perpendicular directions, where carets identify unit vectors. The dimensional position vector for the s/c with respect to O is denoted \vec{R} . (All vectors are denoted with an overarrow.) Within this frame, the dimensional position vector from Earth to the Moon is expressed as \vec{R}_{EM} . The barycenter, i.e., the center of mass between Earth and the Moon, is denoted B , where \vec{B} corresponds to the position vector for B with respect to O . The position vector from B to the s/c is denoted \vec{R}_{Bc} , where subscripts B and c correspond to the barycenter and the s/c, respectively. Then, consider a second frame as illustrated in Fig. 1b, denoting the pulsating–rotating frame, where the origin is now located at B . The unit vectors, $\hat{x} - \hat{y} - \hat{z}$, are constructed as,

$$\hat{x} = \frac{\vec{R}_{EM}}{l}, \quad \hat{y} = \hat{z} \times \hat{x}, \quad \hat{z} = \frac{\vec{h}}{h}, \quad (1)$$

**Fig. 1** Frames under investigation

where l is the magnitude of \vec{R}_{EM} , or the dimensional distance between Earth and the Moon. The angular momentum vector reflecting the primary motion, \vec{h} , is computed as $\vec{h} = \vec{R}_{EM} \times \vec{V}_{EM}$, where \times denotes the cross product and \vec{V}_{EM} is the dimensional velocity expressed in terms of the inertial frame, i.e., $\vec{V}_{EM} = \vec{R}'_{EM} = d\vec{R}_{EM}/dT$, where the prime denotes the derivative with respect to the dimensional time, T . The magnitude of \vec{h} is denoted h . The value for l , or the dimensional distance between Earth and the Moon, pulsates in general as the Earth–Moon motion evolves within the inertial frame. However, the Earth–Moon distance within the pulsating–rotating frame is always nondimensionalized to be unit magnitude. Thus, a unit magnitude distance within the frame correlates to different Earth–Moon distances at different times. Consistent with the rotation of the frame, Earth and the Moon lie on the \hat{x} -axis at fixed positions within the pulsating–rotating frame, $(-\mu, 0, 0)$ and $(1 - \mu, 0, 0)$, respectively. The mass ratio μ is computed as $\mu = \tilde{\mu}_M/(\tilde{\mu}_E + \tilde{\mu}_M)$, where $\tilde{\mu}$ denotes the dimensional gravitational parameter of the respective bodies. Within the pulsating–rotating frame, the nondimensional s/c position vector is represented as $\vec{\rho} = x\hat{x} + y\hat{y} + z\hat{z}$. Then, without losing generality, the relationship between the position vectors within the two frames is retrieved as,

$$\vec{R} = \vec{B} + l\mathbf{C}\vec{\rho}, \quad (2)$$

where the appropriate direction cosine matrix \mathbf{C} is evaluated as, $\mathbf{C} = [\hat{x} \ \hat{y} \ \hat{z}]$. (All matrices are bold.) This relationship is valid for all models under investigation and consists of three components: translation of the origin, \vec{B} , dimensionalization via the pulsating distance, l , and rotation with the direction cosine matrix, \mathbf{C} . These components are generally functions of time and are evaluated at each instant to construct the pulsating frame given the states of the gravitational bodies. The time history of the states is evaluated differently depending on the models. The nondimensional velocity of the s/c, as viewed and expressed in terms of the appropriate frame, is represented by $\dot{\vec{\rho}}$, where the dot represents the differentiation of $\vec{\rho}$ with respect to the nondimensional time, t . Similarly, the nondimensional acceleration of the s/c with respect to the pulsating frame is represented by $\ddot{\vec{\rho}}$. The notations for two independent variables, i.e., T and t , are summarized in Table 1 for clarification.

Table 1 Notations for two independent variables

	Dimensional time (s)	Nondimensional time
Symbol	T	t
Derivative symbol	$\frac{d(\cdot)}{dT} = (\cdot)'$	$\frac{d(\cdot)}{dt} = (\cdot)$
Associated frame	Inertial frame (Fig. 1a)	Pulsating–rotating frame (Fig. 1b)

2.2 Equations of motion

The EOMs for motion of the s/c within the context of the pulsating–rotating frame, i.e., expressions for $\ddot{\vec{\rho}}$, are produced for any models under investigation. To derive the EOMs in a common framework for all the models, differentiate Eq. (2) twice with respect to the dimensional time, T . The first and second derivatives result in the following,

$$\vec{R}' = \vec{B}' + l' \mathbf{C} \vec{\rho} + l \mathbf{C}' \vec{\rho} + l \mathbf{C} \vec{\rho}', \quad (3)$$

$$\vec{R}'' = \vec{B}'' + (l'' \mathbf{C} + 2l' \mathbf{C}' + l \mathbf{C}'') \vec{\rho} + (2l' \mathbf{C} + 2l \mathbf{C}') \vec{\rho}' + l \mathbf{C} \vec{\rho}'', \quad (4)$$

respectively. While this process is consistent with the Newtonian derivation, the Lagrangian derivation is also possible (Gómez et al. 2002). Note that \vec{B}, l, \mathbf{C} are functions of T , in general, and it is natural to include derivatives with respect to dimensional time T . However, as expressions for $\ddot{\vec{\rho}}$ are desired, the transformation between derivatives of $\vec{\rho}$ with respect to dimensional and nondimensional times, i.e., T and t , is detailed. The first and second derivatives are related by,

$$\frac{d\vec{\rho}}{dT} = \vec{\rho}' = \frac{d\vec{\rho}}{dt} \frac{dt}{dT} = \dot{\vec{\rho}} \cdot t' \quad (5)$$

$$\frac{d^2\vec{\rho}}{dT^2} = \vec{\rho}'' = \ddot{\vec{\rho}} \cdot t'^2 + \dot{\vec{\rho}} \cdot t'', \quad (6)$$

respectively. Then, Eq. (4) is solved for $\ddot{\vec{\rho}}$ to render,

$$\begin{aligned} \ddot{\vec{\rho}} = & -\frac{1}{t'} \left[\left(\frac{2l'}{l} + \frac{t''}{t'} \right) \mathbf{I} + 2\mathbf{C}^\top \mathbf{C}' \right] \dot{\vec{\rho}} - \frac{1}{t'^2} \left[\frac{l''}{l} \mathbf{I} + \frac{2l'}{l} \mathbf{C}^\top \mathbf{C}' + \mathbf{C}^\top \mathbf{C}'' \right] \vec{\rho} \\ & + \frac{1}{lt'^2} \mathbf{C}^\top (\vec{R}'' - \vec{B}''), \end{aligned} \quad (7)$$

where superscript \top denotes the transpose of a matrix and \mathbf{I} corresponds to a three-by-three identity matrix. Gómez et al. (2002) also introduce an alternative representation of Eq. (7) with a set of coefficients, i.e., the following form,

$$\ddot{\vec{\rho}} = \begin{bmatrix} b_1 \\ b_2 \\ b_3 \end{bmatrix} + \begin{bmatrix} b_4 & b_5 & 0 \\ -b_5 & b_4 & b_6 \\ 0 & -b_6 & b_4 \end{bmatrix} \dot{\vec{\rho}} + \begin{bmatrix} b_7 & b_9 & b_8 \\ -b_9 & b_{10} & b_{11} \\ b_8 & -b_{11} & b_{12} \end{bmatrix} \vec{\rho} + b_{13} \nabla \Omega, \quad (8)$$

where b_{1-13} correspond to a set of coefficients that are evaluated differently across models but with this same formulation of the EOMs. Note that $\nabla \Omega$ is the gradient of a potential function Ω that is evaluated from,

$$\Omega = \Omega(\mu, \vec{\rho}, \mathcal{A}, \mu_j, \vec{\rho}_j) = \frac{1-\mu}{\rho_{Ec}} + \frac{\mu}{\rho_{Mc}} + \sum_{j \in \mathcal{A}} \frac{\mu_j}{\rho_{jc}}, \quad (9)$$

Table 2 Coefficients in the EOMs for the models under investigation

	HFEM	CR3BP	ER3BP	BCR4BP
b_1	$-\frac{\vec{B}'' \cdot \hat{z}}{(t')^2 l}$	0	0	$-\frac{\mu_S}{\rho_{S,4}^2} \cos \theta_{S,4}$
b_2	$-\frac{\vec{B}'' \cdot \hat{y}}{(t')^2 l}$	0	0	$-\frac{\mu_S}{\rho_{S,4}^2} \sin \theta_{S,4}$
b_3	$-\frac{\vec{B}'' \cdot \hat{z}}{(t')^2 l}$	0	0	0
b_4	$-\frac{l'}{2t'l}$	0	$-\frac{e \sin f}{2\sqrt{1+e \cos f}}$	0
b_5	$\frac{2h}{t'l^2}$	2	$2\sqrt{1+e \cos f}$	2
b_6	$\frac{2l}{t'h} \vec{A}_{EM} \cdot \hat{z}$	0	0	0
b_7	$-\frac{l''}{(t')^2 l} + \frac{h^2}{(t')^2 l^4}$	1	1	1
b_8	$-\frac{1}{(t')^2 l} \vec{A}_{EM} \cdot \hat{z}$	0	0	0
b_9	$\frac{h'}{(t')^2 l^2}$	0	0	0
b_{10}	$-\frac{l''}{(t')^2 l} + \frac{h^2}{(t')^2 l^4} + \frac{l^2}{(t')^2 h^2} (\vec{A}_{EM} \cdot \hat{z})^2$	1	1	1
b_{11}	$\frac{3h' - 2lh'}{(t')^2 h^2} \vec{A}_{EM} \cdot \hat{z} + \frac{l}{(t')^2 h} \vec{J}_{EM} \cdot \hat{z}$	0	0	0
b_{12}	$-\frac{l''}{(t')^2 l} + \frac{l^2}{(t')^2 h^2} (\vec{A}_{EM} \cdot \hat{z})^2$	0	$-e \cos f$	0
b_{13}	$\frac{\tilde{\mu}_E + \tilde{\mu}_M}{l_*^3 (t'_*)^2} = 1$	$\frac{\tilde{\mu}_E + \tilde{\mu}_M}{l_*^3 (t'_*)^2} = 1$	$\frac{\tilde{\mu}_E + \tilde{\mu}_M}{l_*^3 (t'_*)^2} = 1$	$\frac{\tilde{\mu}_E + \tilde{\mu}_M}{l_*^3 (t'_*)^2} = 1$

All symbols are defined as each model is introduced

where the nondimensional gravitational parameter for $j \in \mathcal{A}$, μ_j , is computed as $\mu_j = \tilde{\mu}_j / (\tilde{\mu}_E + \tilde{\mu}_M)$. The different analytical expressions for b_{1-13} for each model are provided in Table 2. These expressions are assessed within the context of the assumptions for each respective model as follows.

2.2.1 HFEM

The HFEM is introduced first, as the expressions for the coefficients in the HFEM apply for other models as well, where the terms simplify depending on the assumptions introduced in the lower-fidelity models. For the HFEM, the set \mathcal{A} is comprised of the Sun and the rest of the significant celestial bodies in the solar system. It is assumed to be a coherent model, where the six-dimensional states and the epoch for the gravitational bodies under their mutual gravitational influence are well approximated by the ephemerides from the SPICE libraries (Acton et al. 2018). For the current analysis, DE440.bsp (Park et al. 2021) is leveraged as the reference ephemerides. Then, the solar system barycenter is the origin, O , for the inertial frame in the HFEM. The analytical expressions for the coefficients for the HFEM are summarized in the second column of Table 2. Note that the coefficients are evaluated with a number of quantities retrieved from the ephemerides. For example, b_{1-3} are related to the acceleration of B within the inertial frame, i.e., $\vec{B}'' = -\sum_{j \in \mathcal{A}} \left(\frac{\tilde{\mu}_j (1-\mu)}{R_{jE}^3} \vec{R}_{jE} + \frac{\tilde{\mu}_j \mu}{R_{jM}^3} \vec{R}_{jM} \right)$, where the barycenter is influenced by the bodies within \mathcal{A} . Additionally, in Table 2, \vec{A}_{EM} and \vec{J}_{EM} correspond to the acceleration and jerk of the Moon with respect to Earth, respectively,

or, $\vec{A}_{EM} = \vec{R}_{EM}''$ and $\vec{J}_{EM} = \vec{R}_{EM}'''$. Note that these quantities are not directly retrieved from the ephemerides, as the SPICE data only include terms up to the first derivative of the position, i.e., the velocity, \vec{V}_{EM} . Thus, these higher-order derivatives are manually constructed assuming the point-mass model for the gravitational bodies. The remaining quantities in the coefficient expressions depend on derivatives of l , h , and t , also constructed from the ephemerides. For detailed derivations for these quantities, refer to Dei Tos (2014). Since the HFEM does not assume a simplified motion for the gravitational bodies, the nondimensional analytical expressions for many coefficients are not necessarily reduced to constants, e.g., one. Rather, they are constructed by the instantaneously retrieved information from the ephemerides depending on T . The time variables T and t are set to zero at a reference epoch, JD_R , corresponding to a Julian date.

2.2.2 CR3BP

For the CR3BP, only the Earth and the Moon are included as the gravitational bodies in the model. The Moon is orbiting around Earth in a circular orbit with a radius of l_* , denoted as the characteristic length. Thus, the Earth–Moon distance (l) for the CR3BP is fixed as a constant quantity, l_* . The characteristic time, $1/t'_*$, is constructed such that $l_*^3(t'_*)^2/(\tilde{\mu}_E + \tilde{\mu}_M) = 1$. Employing Eq. (2) by nondimensionalizing the distance with l_* and time with $1/t'_*$, the following EOMs are produced with respect to the pulsating–rotating frame (Szebehely 1967),

$$\ddot{\vec{\rho}} = -2\hat{z} \times \dot{\vec{\rho}} + \nabla \Omega_C, \quad (10)$$

where Ω_C is the pseudo-potential function for the CR3BP, computed as $\Omega_C = (x^2 + y^2)/2 + \Omega$, then Ω is evaluated with $\mathcal{A} = \emptyset$, or an empty set, since additional gravitational bodies are not included within the CR3BP. The CR3BP depends on only one parameter, μ , and is a time-independent system. In the current work, the μ value is selected to be consistent with the SPICE data. Note that \vec{B} is a zero vector since the barycenter is an inertially fixed point for the CR3BP; it results in $b_{1-3} = 0$, as these terms involve the acceleration of B within the inertial frame, i.e., \vec{B}'' . Many other coefficients are simplified since $l' = h' = 0$, as l and h do not vary for a circular orbit of the Moon around Earth, as assumed in the CR3BP. Therefore, a majority of the coefficients simplify to zeros, except the following notable terms: $b_5 = 2$ (Coriolis), $b_7 = b_{10} = 1$ (centrifugal), and $b_{13} = 1$ (gravity from the primaries). Note that the dimensional quantity l_* does not appear in the CR3BP; it does not impact the dynamics within the pulsating–rotating frame.

2.2.3 ER3BP

The ER3BP assumes a conic orbit for the Moon around Earth, where no additional gravitational bodies are present, or, $\mathcal{A} = \emptyset$. For the initial derivation, the semi-major axis for the conic is assumed to be l_* , the characteristic length for the CR3BP, with an eccentricity value of e . Introducing a new independent variable, then, the following EOMs are developed with respect to the true anomaly, f (Szebehely 1967), i.e.,

$$\frac{d^2 \vec{\rho}}{df^2} = -2\hat{z} \times \frac{d\vec{\rho}}{df} + \nabla \Omega_E, \quad (11)$$

where Ω_E is the pseudo-potential function for the ER3BP, evaluated as $\Omega_E = \frac{1}{1+e\cos f}\Omega_C - \frac{e\cos f}{1+e\cos f} \cdot \frac{z^2}{2}$. Switching the independent variable from f to the nondimensional time t , the EOMs for the ER3BP are derived as,

$$\ddot{\vec{\rho}} = -\frac{e\sin f}{2\sqrt{(1+e\cos f)}}\dot{\vec{\rho}} - 2\hat{z} \times \dot{\vec{\rho}}\sqrt{1+e\cos f} - e\cos f z\hat{z} + \nabla\Omega_C, \quad (12)$$

where the added complexities are apparent in comparison to the CR3BP, as the Earth–Moon distance (l) is not constant as modeled within the ER3BP. As a result, some of the coefficients from Table 2 are evaluated with terms containing e and f , but note that the expressions are much simpler in contrast to the HFEM. The relative simplicity is due to the fact that a conic orbit leads to $h' = 0$. Similar to the CR3BP, as additional bodies are not present, B is considered an inertially fixed point and b_{1-3} are still zeros. Yet, due to the appearance of f in the EOMs, the ER3BP is a time-dependent system where $\dot{f} = \sqrt{1+e\cos f}$ with a period of 2π radians in f . Similar to the CR3BP, the semi-major axis for the eccentric orbit of the Moon around the Earth does not impact the dynamics, as the EOMs are represented in the nondimensional pulsating–rotating frame. Also, μ is constructed as the same value as that of the CR3BP. Thus, an ER3BP in the current investigation is fully defined by two variables: one parameter, e , as well as the reference value for the true anomaly, f_R . As the ER3BP is a time-dependent system, a nonzero reference value f_R is potentially assigned for the reference epoch from the HFEM, JD_R , where $T = t = 0$.

2.2.4 BCR4BP

The BCR4BP incorporates the solar gravity into the CR3BP dynamics. While multiple formulations exist for the BCR4BP, the planar BCR4BP is leveraged in the current investigation. In addition to the assumptions in the CR3BP, the planar BCR4BP models the Sun and B both as following circular paths around their mutual barycenter, B_S , where all the gravitational bodies are moving in the same plane. The term “BCR4BP” is utilized to denote the planar BCR4BP in the current work; note that different formulations for the BCR4BP result in different EOMs and, thus, different coefficients in Table 2. By assumption, the Sun does not exert a gravitational force on Earth and the Moon directly, but it influences B ; thus, the BCR4BP is not a coherent model. The constant, nondimensional distance between the Sun and B is denoted $\rho_{S,4}$, where ‘4’ denotes the BCR4BP. Then, the nondimensional position vector of the Sun within the pulsating–rotating frame is expressed as, $\vec{\rho}_{S,4} = \rho_{S,4} \cos \theta_{S,4} \hat{x} + \rho_{S,4} \sin \theta_{S,4} \hat{y}$, where $\theta_{S,4}$ denotes the angle between \hat{x} -axis and $\vec{\rho}_{S,4}$, also labeled the Sun angle. The Sun angle changes at a constant rate in the BCR4BP, or, $\dot{\theta}_{S,4} = n_S - 1$, where $n_S = \sqrt{\frac{\tilde{\mu}_S + \tilde{\mu}_E + \tilde{\mu}_M}{(\tilde{\mu}_E + \tilde{\mu}_M)\rho_{S,4}^3}}$.

This angular rate is negative, i.e., the Sun appears to rotate in the clockwise direction as viewed in the Earth–Moon $\hat{x} - \hat{y}$ plane. The EOMs representing the BCR4BP within the pulsating–rotating frame yield (Scheuerle 2021),

$$\ddot{\vec{\rho}} = -2\hat{z} \times \dot{\vec{\rho}} + \nabla\Omega_4, \quad (13)$$

where Ω_4 is the pseudo-potential function for the BCR4BP, evaluated as $\Omega_4 = (x^2 + y^2)/2 + \Omega - \Omega_{S,B}$. The potential function Ω is formulated with $\mathcal{A} = \{\text{Sun}\}$. Note that the last term, $\Omega_{S,B} = \mu_S/\rho_{S,4}^2(x \cos \theta_{S,4} + y \sin \theta_{S,4})$, originates from the gravitational acceleration of B due to the Sun, or,

$$\nabla\Omega_{S,B} = \frac{1}{l_*^2 t_*'} \mathbf{C} \vec{B}'' = -\frac{\tilde{\mu}_S}{l_*^2 t_*'} \frac{\mathbf{C} \vec{R}_{SB}}{R_{SB}^3} = \frac{\mu_S}{\rho_{S,4}^3} \vec{\rho}_{S,4}. \quad (14)$$

Thus, the coefficients b_{1-2} for the BCR4BP are nonzero and depend on the location of the Sun within the pulsating–rotating frame. The rest of the coefficients for the BCR4BP are the same as in the CR3BP, as l and h in the BCR4BP are also constant. These constants occur by adding the Sun to the CR3BP in a manner that is not coherent, i.e., where the Moon remains in a circular orbit around Earth despite the presence of the Sun. Yet, the BCR4BP is a time-dependent system where the nondimensional period is $2\pi/(1 - n_S)$. The BCR4BP is fully defined by one parameter, $\rho_{S,4}$, as well as the reference epoch, $\theta_{S,4,R}$, that corresponds to JD_R from the HFEM. Note that μ and $\tilde{\mu}_S$ are consistently defined from the ephemerides and do not count as additional parameters.

2.3 Isochronous correspondence

While the EOMs from Eq. (8) provide a methodology to assess the dynamical models in a consistent formulation, the evaluation of the coefficients in Table 2 requires a definition for the relationship between the independent variables in the different models. For example, while the CR3BP EOMs in Eq. (10) evolve with the nondimensional time, t , the bodies within the HFEM depend on the dimensional time, T , as retrieving the SPICE data requires an epoch expressed in terms of T . Thus, formulating the EOMs for the HFEM with respect to t requires a definition for $t' = dt/dT$, a quantity that appears frequently in the expressions for b_{1-13} . It is emphasized that t' may be defined by any arbitrary function, as the CR3BP and HFEM are constructed independently; the expression for t' does not change the dynamical evolution in the models but delivers a suitable isochronous correspondence between the various models.

While there exists no precise definition for t' , one formulation may be preferred over another for some numerical properties. One possible option for t' is an assumption to render a uniform flow of time, i.e.,

$$\text{Uniform flow of time } t' = t_*' = \sqrt{\frac{\tilde{\mu}_E + \tilde{\mu}_M}{l_*^3}}, \quad (15)$$

where l_* is the constant, characteristic length from the CR3BP. One advantage of this formulation is the simplicity in computing $t'' = 0$ that appears in expressions for the coefficients that are related to $\dot{\rho}$, i.e., $b_{7,10,12}$. Thus, the constant flow of time is typically adopted in previous investigations (Gómez et al. 2002; Dei Tos and Topputo 2017a; Hou and Liu 2010) leveraging the EOMs within the pulsating–rotating frame. However, one noticeable drawback of this formulation is that, as the distance l pulsates, the quantity $l^3(t'_*)^2/(\tilde{\mu}_E + \tilde{\mu}_M)$ does not equal one. Here, Gómez et al. (2001) note that a coherence problem then occurs, as in the CR3BP, the core property of the nondimensionalization process is that $l_*^3(t'_*)^2/(\tilde{\mu}_E + \tilde{\mu}_M) = 1$. As a consequence, when utilizing $t' = t'_*$ under a realistic pulsation of the primaries, the coefficient for the gravity from the primaries, b_{13} , is not consistently scaled to one but depends on the distance between the primaries.

In response to this coherence problem, in the current work, a non-uniform flow of time is adopted as an alternative. The relationship between t and T is defined as follows,

$$\text{Non-uniform flow of time } t' = \sqrt{\frac{\tilde{\mu}_E + \tilde{\mu}_M}{l^3}}, \quad (16)$$

where t' is now a function of the pulsating distance, l , and automatically satisfies $l^3(t')^2/(\tilde{\mu}_E + \tilde{\mu}_M) = 1$. As a result, b_{13} is consistently evaluated as unity for all models under investigation. Utilizing this non-uniform flow of time also aids in the proper scaling

for the transformation of the states between the inertial and pulsating–rotating frames. The following expression summarizes the transformation,

$$\begin{bmatrix} \vec{R} - \vec{B} \\ \vec{R}' - \vec{B}' \end{bmatrix} = \begin{bmatrix} l\mathbf{C} & \mathbf{0}_{3 \times 3} \\ l'\mathbf{C} + l\mathbf{C}' & l\mathbf{C} \cdot t' \end{bmatrix} \begin{bmatrix} \vec{\rho} \\ \dot{\vec{\rho}} \end{bmatrix}, \quad (17)$$

where the rows correspond to Eqs. (2) and (3), respectively. For given initial conditions in the CR3BP, i.e., $(\vec{\rho}_0, \dot{\vec{\rho}}_0)$, the initial guess within the HFEM is often delivered from the above equation (Ocampo 2003; Oguri et al. 2020). It is noted that the dimensional inertial velocity expression, $\vec{R}' - \vec{B}'$, includes a term that scales $\dot{\vec{\rho}}$ by t' . Indeed, the initial guess for the velocity in the HFEM is inseparable from the relationship between the independent time variables, i.e., t' . Note that $(\vec{\rho}_0, \dot{\vec{\rho}}_0)$ evolves under the CR3BP dynamics and, intuitively, leveraging Eq. (16) aids in generating an initial guess in the HFEM that maintains the characteristics in the original CR3BP solution, as noted by many authors (Oguri et al. 2020; Ocampo 2003; Olikara 2016; Park 2021). For the current investigation, it is desired to identify additional forces in the HFEM with respect to the CR3BP by writing the EOMs in the common formulation. Thus, a choice of t' that results in relatively small deviations of the coefficients between the HFEM and CR3BP facilitates the analysis and Eq. (16) is, thus, adopted. It automatically satisfies $l^3(t')^2/(\tilde{\mu}_E + \tilde{\mu}_M) = 1$; therefore, the coefficient for the gravity of the primaries, i.e., b_{13} , is consistently evaluated as unity, and velocity is also consistently scaled such that the difference in the coefficients is likely to be reduced. One small complexity in this formulation is the nonzero value of the t'' term. It is computed as $t'' = -\sqrt{(\tilde{\mu}_E + \tilde{\mu}_M)/l^5}l' = -3t'l'/2l$ and is straightforward to evaluate.

The potential impact of these two different relationships, i.e., t' and t'_* , on the transition process is illustrated in Fig. 2a. The gray plot in Fig. 2a illustrates the planar projection of a three-dimensional L₂ halo orbit with a period of 14.8 days as represented within the pulsating–rotating frame, computed within the CR3BP. The gray dot corresponds to the initial state $(\vec{\rho}_0, \dot{\vec{\rho}}_0)$ along the sample orbit. This state is propagated within the HFEM over one half-period originating from two different initial epochs. Figure 2b illustrates the time history for the Earth–Moon distance, l , in the HFEM over 1 year originating at 09/23/2022, where the red line corresponds to the constant l_* value as employed in the CR3BP. The quantity displays a quasi-periodic behavior, where the sample date and range (1 year) represent an arbitrary set of numbers. Over this range, two epochs are selected, where the blue dot corresponds to the epoch when the Earth–Moon distance is maximized for the given range of epochs, and the orange dot corresponds to the minimum value of l . Then, four colored lines in Fig. 2a correspond to propagated results initiated from the same state, $(\vec{\rho}_0, \dot{\vec{\rho}}_0)$, where the colors represent the initial epoch. The solid lines correspond to the HFEM propagation with coefficients constructed using the non-uniform flow of time (Eq. (16)), and the dotted lines correspond to the uniform flow of time (Eq. (15)). Although all four lines eventually depart from the original CR3BP orbit, it is apparent that the HFEM paths constructed with the non-uniform t' are more resilient to the pulsation of l by automatically enforcing $l^3(t')^2/(\tilde{\mu}_E + \tilde{\mu}_M) = 1$. Alternatively, for t'_* , when $l = l_{max}$, the initial velocity tends to be over-scaled, and vice versa, resulting in noticeable deviations from the original geometry designed in the CR3BP. It is observed that this simple propagation does not necessarily predict the performance of the subsequent transitions into the HFEM, where the “errors” in the propagation are often successfully mitigated by differential correctors. However, it is emphasized again that this revised expression for t' aids in consistent scaling for both velocity components in transformation and the coefficients, b_{1-13} . The utilization of this updated formulation for t' marks a significant departure from earlier studies (Gómez et al. 2002; Dei Tos and Toppo

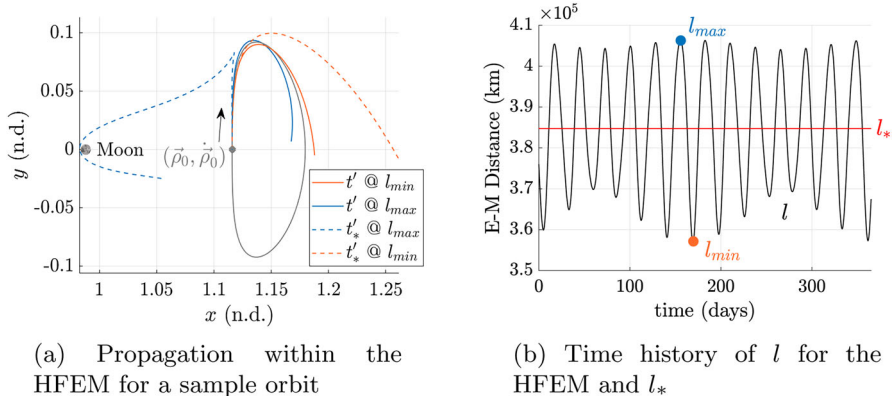


Fig. 2 An illustrative example for the impact of t' on velocity scaling

2017a; Hou and Liu 2010), and facilitates the identification of valuable patterns within the HFEM dynamics as detailed in Sect. 3.

For completeness, the isochronous correspondence for the independent variables in the remaining two models, i.e., the ER3BP and the BCR4BP, is also important. For the ER3BP, the following relationship between f and t is constructed,

$$\dot{f} = \frac{f'}{t'} = \frac{h_E}{l_E^2} \sqrt{\frac{l_E^3}{\tilde{\mu}_E + \tilde{\mu}_M}} = \sqrt{1 + e \cos f}, \quad (18)$$

where h_E and l_E are the angular momentum and the Earth–Moon distance for the assumed conic motion of the Moon around Earth. The conic equation, i.e., $l_E = h_E^2 / ((\tilde{\mu}_E + \tilde{\mu}_M) \cdot (1 + e \cos f))$, is leveraged for the derivation. Under this definition for f , the expressions for b_{1-13} in Table 2 for the ER3BP are not explicitly dependent on l_E . For the BCR4BP, it is straightforward to assume that the independent variable for the BCR4BP is the same as that of the CR3BP.

3 Analysis of the HFEM

The EOMs from Eq. (8) supply a common formulation of the dynamical models, where the coefficients b_{1-13} are evaluated differently for each model. As apparent from the expressions in Table 2, the HFEM coefficients consist of quantities that depend on time. The time history for the coefficients in the HFEM appear in Fig. 3 over 1 year originating on 09/23/2023. Two coefficients are not included in the figure; b_{10} typically differs from b_7 by a very small amount that is not apparent visually in the scale of Fig. 3c, and b_{13} is computed as a constant number, i.e., one. As the coefficients for the HFEM display complex behavior, it is non-trivial to deduce simple patterns that aid in understanding the HFEM as a perturbed model of the CR3BP. In response to this problem, previous investigations focus on identifying multiple core frequencies in the coefficients via Fourier analysis (Gómez et al. 2002; Dei Tos and Topputto 2017a). However, since leveraging multiple frequencies simultaneously is difficult, it is beneficial to determine the most dominant frequency to gain better insights into the transition problem and assess the potential application of one-frequency intermediate models. This task remains challenging, as the analysis is dependent on a number of factors including

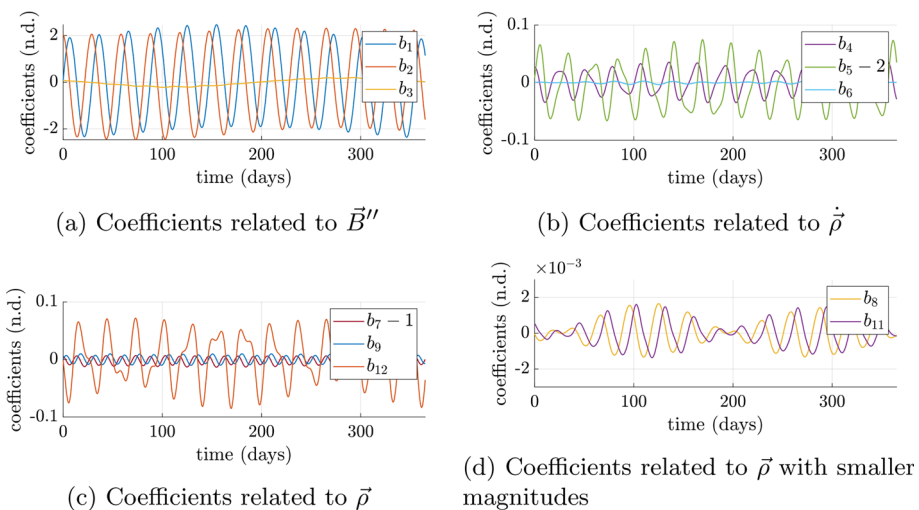


Fig. 3 Time history for the coefficients in the HFEM beginning 09/23/2023 and ranging over 1 year

the specific epoch and spacecraft state. Currently, there is no agreement on the most dominant source of acceleration and the associated frequency within the context of transitioning Earth–Moon CR3BP solutions into the HFEM, and different conclusions are presented by various authors (Gómez et al. 2002; Dei Tos and Topputto 2017a).

The current work adopts an analytical approach to further reduce the complexity of the expressions in Table 2. The coefficients are categorized into two sources: the pulsation of the Earth–Moon system and gravity from additional gravitational bodies, e.g., the Sun, generating recognizable patterns. These sources exhibit different dominant frequencies, facilitating the subsequent assessment of one-frequency intermediate models in Sect. 4. Relative magnitudes of accelerations originating from these two sources are visually represented for an in-plane s/c motion within the Earth–Moon plane, highlighting the most dominant frequency as a function of the s/c state.

3.1 Rearranging the HFEM EOMs

The EOMs for the HFEM are rearranged such that cancellations occur among the complex coefficients and also highlight the impact of the additional forces. The accelerations in the HFEM are initially categorized relevant to the three sources: (1) CR3BP, (2) pulsation, and (3) additional bodies, i.e.,

$$\ddot{\vec{\rho}}_H = \ddot{\vec{\rho}}_C + \ddot{\vec{\rho}}_{P,H} + \ddot{\vec{\rho}}_{\mathcal{A},H} \quad (19)$$

where the subscripts H , C , P , and \mathcal{A} denote the HFEM, CR3BP, pulsation, and additional bodies, respectively. Note that Eq. (19) is consistent with the isochronous correspondence defined by Eq. (16). This categorization of the terms is somewhat arbitrary, as the “true” pulsation is indeed inseparable from the gravitational influence due to the additional bodies. As the ER3BP incorporates a conic pulsation with $\mathcal{A} = \emptyset$, the additional terms in the ER3BP, as compared to the CR3BP, are initially identified as the acceleration originating from pulsation. Observing the coefficients in the CR3BP and ER3BP, the pulsation acceleration is

defined as,

$$\ddot{\vec{\rho}}_P := \ddot{\vec{\rho}}_E - \ddot{\vec{\rho}}_C = \begin{bmatrix} b_4 & b_5 - 2 & 0 \\ -b_5 + 2 & b_4 & 0 \\ 0 & 0 & b_4 \end{bmatrix} \dot{\vec{\rho}} + \begin{bmatrix} 0 & 0 & 0 \\ 0 & 0 & 0 \\ 0 & 0 & b_{12a} \end{bmatrix} \vec{\rho}, \quad (20)$$

where the subscript E denotes the ER3BP. These additional terms consist of $b_{4,5,12a}$ that are evaluated differently for the ER3BP and HFEM to retrieve $\ddot{\vec{\rho}}_{P,E}$ and $\ddot{\vec{\rho}}_{P,H}$, respectively. The coefficient b_{12a} is the first term in b_{12} , evaluated as $b_{12a} = -l''/(r^2 l)$. These coefficients are primarily dependent on l, l' and l'' , i.e., the quantities that are related to pulsation. As the BCR4BP does not incorporate pulsation into the model, this acceleration is evaluated as zero in the BCR4BP. The remaining perturbing accelerations are then grouped and represented as originating from the inclusion of additional bodies, or,

$$\ddot{\vec{\rho}}_{\mathcal{A}} := \ddot{\vec{\rho}}_H - \ddot{\vec{\rho}}_C - \ddot{\vec{\rho}}_P = \begin{bmatrix} b_1 \\ b_2 \\ b_3 \end{bmatrix} + \begin{bmatrix} 0 & 0 & 0 \\ 0 & 0 & b_6 \\ 0 & -b_6 & 0 \end{bmatrix} \dot{\vec{\rho}} + \begin{bmatrix} b_7 - 1 & b_9 & b_8 \\ -b_9 & b_{10} - 1 & b_{11} \\ b_8 & -b_{11} & b_{12} - b_{12a} \end{bmatrix} \vec{\rho} + \nabla \sum_{j \in \mathcal{A}} \frac{\mu_j}{\rho_{jc}}, \quad (21)$$

where some of the terms are now approximated in the BCR4BP. In contrast, the ER3BP includes a zero acceleration for $\ddot{\vec{\rho}}_{\mathcal{A}}$ as additional bodies are not present in the model. Although grouping the rest of the terms is arbitrary to some degree, manipulation of Eq. (21) results in much simplified expressions that are dominated by the quantities associated with the additional bodies. Following the derivations in Appendix A, the equation is rewritten as,

$$\ddot{\vec{\rho}}_{\mathcal{A},H} = \ddot{\vec{\rho}}_{\mathcal{A},G} + \begin{bmatrix} 0 & 0 & 0 \\ 0 & 0 & b_6 \\ 0 & -b_6 & 0 \end{bmatrix} \dot{\vec{\rho}} + \begin{bmatrix} 0 & 0 & 0 \\ 0 & b_{12} - b_{12a} & b_{11} \\ 0 & -b_{11} & b_{12} - b_{12a} \end{bmatrix} \vec{\rho}, \quad (22)$$

where $\ddot{\vec{\rho}}_{\mathcal{A},G}$ denotes the “pseudo-gravity” term from Appendix A, evaluated as,

$$\ddot{\vec{\rho}}_{\mathcal{A},G} = - \sum_{j \in \mathcal{A}} \mu_j \left(\frac{\vec{\rho}_{jc}}{\rho_{jc}^3} + \frac{\vec{\rho}_{Mc} \cdot \hat{x}}{\rho_{jE}^3} \vec{\rho}_{jE} - \frac{\vec{\rho}_{Ec} \cdot \hat{x}}{\rho_{jM}^3} \vec{\rho}_{jM} - \frac{\vec{\rho}_{Mc} \cdot \hat{y}}{\rho_{jE}^3} (\vec{\rho}_{jE} \times \hat{z}) \right. \\ \left. + \frac{\vec{\rho}_{Ec} \cdot \hat{y}}{\rho_{jM}^3} (\vec{\rho}_{jM} \times \hat{z}) - \left(\frac{zz_j}{\rho_{jE}^3} - \frac{zz_j}{\rho_{jM}^3} \right) \hat{x} \right). \quad (23)$$

The significance of this expression is that the terms only depend on $\vec{\rho}_j$ and $\vec{\rho}$, or, the position vectors of the additional bodies and the s/c in the pulsating–rotating frame, as the primaries are fixed within this frame. The terms also include the inverse cubes of the distance between the bodies; hence, they are labeled as the pseudo-gravity term. Many of the original expressions for the coefficients in Eq. (21) cancel to result in this simplified formulation; as the HFEM is assumed to be a coherent model, the coefficients all essentially originate from the mutual gravitational influences of the bodies. While the cancellation happens between b_{1-3}, b_{7-10} and $\nabla \sum_{j \in \mathcal{A}} (\mu_j / \rho_{jc})$, the remaining terms do not necessarily transform into simple expressions. These terms correspond to $b_{6,11}$, and $b_{12} - b_{12a}$ in Eq. (22). While these coefficients involve some non-trivial terms that are challenging to evaluate, e.g., $\vec{J}_{EM} \cdot \hat{z}$, they are typically associated with relatively small magnitudes as compared to the other coefficients, as apparent in Fig. 3. Also, the pseudo-gravity acceleration involves pairs of similar expressions that reflect the subtraction of terms dependent on $\vec{\rho}_{jM}$ from terms involving $\vec{\rho}_{jE}$. Noting these characteristics, Eq. (22) is further simplified with the following assumptions:

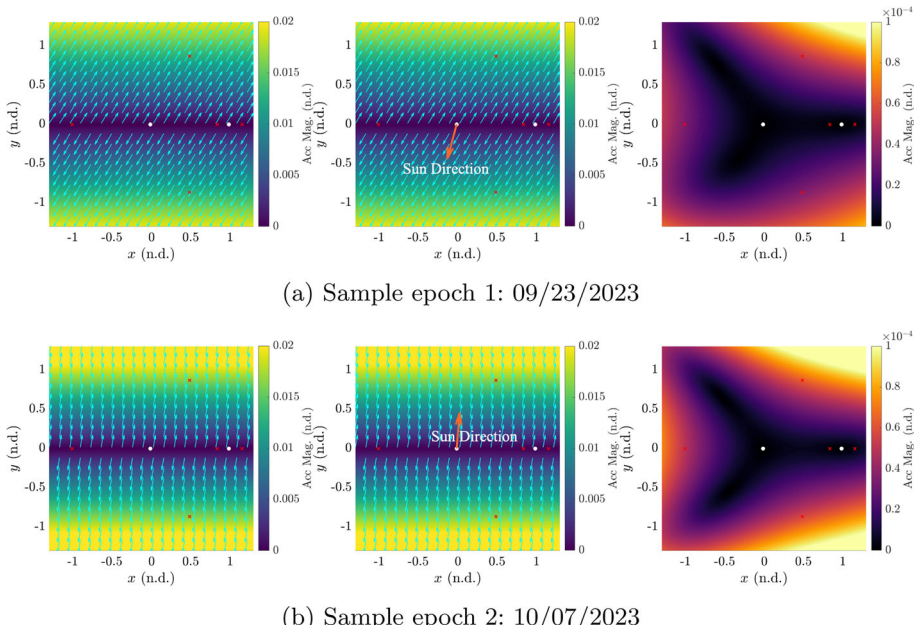


Fig. 4 Contour plots for $\ddot{\rho}_{\mathcal{A},L}$ (left), $\ddot{\rho}_{\mathcal{A},H}$ (center), and $\ddot{\rho}_{\mathcal{A},H} - \ddot{\rho}_{\mathcal{A},L}$ (right)

(1) the additional bodies exert negligible forces except the Sun, (2) the Sun is far from B , i.e., $\rho_S >> 1$, and (3) the out-of-plane component of the Sun's position within the pulsating–rotating frame is negligible in comparison to the in-plane components, or, $|z_S| \ll \rho_S$. Then, as deduced from the derivations in Appendix B, Eq. (22) is simplified as,

$$\ddot{\rho}_{\mathcal{A},H} \approx \ddot{\rho}_{\mathcal{A},L} = \frac{3\mu_S}{\rho_S^5} (2x_S y_S y \hat{x} + (y_S^2 - x_S^2) y \hat{y}), \quad (24)$$

where the subscript L denotes linearization. Assuming that $\rho_S^2 \approx x_S^2 + y_S^2$, or the out-of-plane component of the Sun's position is negligible, $\ddot{\rho}_{\mathcal{A},L} \approx 3\mu_S/\rho_S^3|y|$, i.e., the magnitude of the solar perturbation varies linearly with the y -excursion of the s/c within the pulsating–rotating frame. Denoting the Sun's position vector as $\vec{\rho}_S \approx \rho_S \cos \theta_S \hat{x} + \rho_S \sin \theta_S \hat{y}$, where θ_S is the Sun angle that is defined consistent with the BCR4BP ($\theta_{S,4}$), Eq. (24) is equivalently expressed as,

$$\ddot{\rho}_{\mathcal{A},L} \approx \frac{3\mu_S}{\rho_S^3} y (\sin 2\theta_S \hat{x} - \cos 2\theta_S \hat{y}), \quad (25)$$

where it is notable that $2\theta_S$ appears in the trigonometry functions. To validate this result, consider the contour plots in Fig. 4, corresponding to $\ddot{\rho}_{\mathcal{A},L}$, $\ddot{\rho}_{\mathcal{A},H}$, and the difference between the two accelerations. These acceleration expressions are investigated at multiple points constructed within the $\hat{x} - \hat{y}$ plane, assuming that z and \dot{z} are both zero in magnitude and the zero vector, respectively. In the plots, the white circles denote the primaries, i.e., Earth and the Moon and the red x's correspond to the five Lagrange points. The color in the plots denotes the acceleration magnitude computed at each location, and the cyan arrows note the direction of the acceleration vector. The contour plots in Fig. 4a correspond to an epoch on 09/23/2023, when $\theta_S \approx -105^\circ$, as illustrated by an orange arrow aligned with

the direction of the Sun within the frame. From the plots, it is notable that the linearized acceleration, $\ddot{\rho}_{A,L}$, is closely aligned with the original acceleration direction, $\ddot{\rho}_{A,H}$, where the differences are orders of magnitude smaller as compared to the scale of $\ddot{\rho}_{A,H}$. Another epoch is considered in Fig. 4b, corresponding to an epoch on 10/07/2023 associated with $\theta_S \approx 85^\circ$. Note that while the specific patterns for the difference between linearized and nonlinear accelerations, i.e., $\ddot{\rho}_{A,H} - \ddot{\rho}_{A,L}$, vary across epochs, the maximum discrepancy is constructed at a similar level, approximately on the order of $1 \cdot 10^{-4}$ nondimensional unit (n.d.). Approximately, the magnitude varies linearly with the y -excursion of the s/c, resulting in negligible perturbing accelerations near the \hat{x} -axis but more significant in the L_{4,5} regions, where the y -excursion is approximately 0.87 n.d.. In these regions, the acceleration magnitude exceeds 0.01 n.d., comparable to an acceleration level that a low-thrust engine is able to provide, e.g., Intuitive Machine's Khon-1 s/c (Hoffman et al. 2022), which also approximately produces an acceleration level of 0.01 n.d., implying a non-negligible acceleration magnitude. The direction of the acceleration is then computed as,

$$\arctan_2(-\text{sgn}(y) \cos 2\theta_S, \text{sgn}(y) \sin 2\theta_S) = -\text{sgn}(y) \cdot 90^\circ + 2\theta_S, \quad (26)$$

where \arctan_2 is a four quadrant arctangent and sgn is a sign function. From the plots, it is apparent that the cyan arrows generally align with the above angles. While the form in Eq. (25) is counter-intuitive, it indeed represents the gravitational influence of the Sun on the s/c in the pulsating–rotating frame under a *coherent model*.

3.2 Frequency information

The frequency information from Gómez et al. (2002) is reviewed and applied to the current analysis. They introduce five fundamental frequencies that represent the time-dependent accelerations from the Sun–Earth–Moon HFEM, cast within the pulsating–rotating frame. Two of these frequencies, measured in the constant non-dimensional time unit defined as Tt'_* , correspond to: (1) $v_{1*} \approx 0.9915$, the pulsation frequency associated with the anomalistic month, computed as the difference between the frequency of the mean longitude of the Moon (sidereal frequency, typically constructed to be 1) and the frequency of the lunar perigee, and (2) $v_{2*} \approx 0.9250$, the synodic frequency, associated with the mean elongation of the measured relative to the Sun. The subscript $*$ denotes that the frequencies are defined in the *constant* time domain, or t_* -domain, utilizing the uniform isochronous definition from Eq. (15).

It is then observed that the grouping of the terms in Eq. (19) is supported by the fact that they are mainly described by distinct frequencies. The first group of terms, $\ddot{\rho}_C$, represents the acceleration components that are equivalent to the CR3BP dynamics and time-independent. The other groups of terms, $\ddot{\rho}_{P,H}$ and $\ddot{\rho}_{A,H}$, are time-dependent acceleration terms. For the acceleration terms that result from pulsation, or $\ddot{\rho}_{P,H}$, the coefficients are quasi-periodic functions where the frequency associated with the largest amplitude corresponds to v_{1*} . Recall that these coefficients, $b_{4,5,12a}$, are mainly associated with the Earth–Moon distance, l . Approximating these quasi-periodic quantities with trigonometric series of order 1 results in,

$$l(T) \approx l_{0*} - l_{1*} \cos \theta_{1*} \quad (27)$$

$$b_4(T) \approx b_{4,0*} - b_{4,1*} \sin \theta_{1*} \quad (28)$$

$$b_5(T) \approx b_{5,0*} + b_{5,1*} \cos \theta_{1*} \quad (29)$$

$$b_{12a}(T) \approx b_{12a,0*} - b_{12a,1*} \cos \theta_{1*}. \quad (30)$$

Table 3 Coefficients for the fitted function utilizing v_{1*}

	Q_{0*}	Q_{1*}	E (%)
l	3.8500×10^5 km	2.0905×10^4 km	27
b_4	1.9111×10^{-8} n.d.	2.6925×10^{-2} n.d.	33
b_5	1.9938 n.d.	5.3735×10^{-2} n.d.	35
b_{12a}	3.1686×10^{-3} n.d.	5.2889×10^{-2} n.d.	41

The phase angle is represented as $\theta_{1*} = v_{1*} T t_* + \theta_{1*,R}$, where $\theta_{1*,R}$ denotes the reference phase angle associated with the reference epoch, JD_R . Note that the time-varying quantities are approximated with the same dominant frequency, v_{1*} , and the reference phase angle $\theta_{1*,R}$. Higher frequencies corresponding to multiples of v_{1*} are ignored for simplicity in the current analysis. The coefficients for the approximated functions are included in Table 3, where the *fit* function from MATLAB R2019b (The MathWorks Inc. 2019) is utilized to retrieve quantities that minimize the mean squared error between the true values and the fitted values. A sufficiently large number of samples (2^{20}) that are evenly placed in T are retrieved, where the total time spans between 01/01/1550 and 01/01/2500. In Table 3, Q_{0*} and Q_{1*} denote the zeroth- and first-order coefficients for the fitted functions from Eqs. (27)–(30). The last column of the table represents the maximum relative error, E , resulting from the approximation with a single frequency. For instance, the error for the Earth–Moon distance, l , is computed as $\Delta l_* := l - l_{0*} - l_{1*} \cos \theta_{1*}$. Then, the maximum relative error is defined as, $E := \max(\Delta l_*/(\Delta l_* + l_{1*}))$. The value 27% implies that the unmodeled oscillations from the original expression remain relatively small when the dominant frequency is incorporated. It is apparent that Eqs. (27)–(30) represent more than 50% of the time-varying components of each quantity associated with $\ddot{\rho}_{P,H}$, implying that v_{1*} is indeed the governing frequency for these quantities. The unmodeled oscillatory terms are associated with multiples of v_{1*} and linear, integer combinations of the five frequencies that include v_{1*} and v_{2*} . For these secondary terms, refer to the Fourier analysis results that appear in Gómez et al. (2001).

As multiple dynamical models are written with respect to the nondimensional time t that is constructed with the non-uniform isochronous relationship from Eq. (16), it is beneficial to consider the fitted functions in the t -domain. Similar to the previous case, 2^{20} samples, that are equally placed in t , are selected. As accessing the ephemerides requires the specific *dimensional* time, or T , the corresponding T value at each t is computed via following relationship,

$$T(t) = \int_0^t \sqrt{\frac{l(T)^3}{\tilde{\mu}_E + \tilde{\mu}_M}} dt, \quad (31)$$

utilizing an explicit integration scheme that integrates Eq. (16). Then, Eqs. (27)–(30) are rewritten as,

$$l(t) \approx l_0 - l_1 \cos \theta_1 \quad (32)$$

$$b_4(t) \approx b_{4,0} - b_{4,1} \sin \theta_1 \quad (33)$$

$$b_5(t) \approx b_{5,0} + b_{5,1} \cos \theta_1 \quad (34)$$

$$b_{12a}(t) \approx b_{12a,0} - b_{12a,1} \cos \theta_1, \quad (35)$$

where $\theta_1 = v_1 t + \theta_{1,R}$ corresponds to the phase angle with respect to the nondimensional time t . The updated dominant frequency corresponds to, $v_1 = 0.9896$ n.d., denoted as the

Table 4 Coefficients for the fitted function utilizing ν_1

	Q_0	Q_1	E (%)
l	3.8500×10^5 km	2.0905×10^4 km	26
b_4	1.9111×10^{-8} n.d.	2.6925×10^{-2} n.d.	30
b_5	1.9938 n.d.	5.3735×10^{-2} n.d.	32
b_{12a}	3.1686×10^{-3} n.d.	5.2889×10^{-2} n.d.	39

HFEM pulsation frequency in the current investigation. This value is slightly smaller as compared to ν_{1*} , where the discrepancy is expected from the fact that the transformation of the independent variables leverages a non-uniform relationship as defined in Eq. (16). While the coefficients for the fitted functions are slightly adjusted as apparent in Table 4, a similar tendency exists where ν_1 remains the dominant frequency for the acceleration terms that are identified to be originating from pulsation, $\ddot{\rho}_{P,H}$.

A similar analysis is conducted for the acceleration originating from the additional bodies. The full representation of the acceleration corresponds to Eq. (22), associated with terms that do not simplify, e.g., $b_{6,11}$. Noting that these terms are mainly associated with the out-of-plane direction acceleration and are typically smaller in magnitude, the simplified expression, $\ddot{\rho}_{A,L}$, is utilized to represent the acceleration. From Eq. (24), it is observed that the magnitude of the acceleration is most relevant to the nondimensional solar distance from the barycenter, ρ_S , and the direction is governed by x_S and y_S , or the solar position components within the Earth–Moon plane. The synodic frequency ν_{2*} is leveraged to construct the following approximations for the relevant quantities,

$$\rho_S(T) \approx \rho_{S*} \quad (36)$$

$$x_S(T) \approx \rho_{S*} \cos \theta_{2*} \quad (37)$$

$$y_S(T) \approx \rho_{S*} \sin \theta_{2*}, \quad (38)$$

where $\theta_{2*} = -\nu_{2*} T t_* + \theta_{2*,R}$. Note that this angle is defined such that it decreases over time to represent the clockwise solar motion within the Earth–Moon pulsating rotating frame. As ρ_S leverages the Earth–Moon distance l for its computation, the most dominant oscillation of ρ_S varies with ν_{1*} ; however, it is approximated as a constant value, $\rho_{S*} \approx 389$ (n.d.) as the direction information requires ν_{2*} , considered to be more important for a proper modeling. The maximum relative errors, E , for the approximated x_S and y_S correspond to 17% and 15%, noting that the solar acceleration direction is well represented by the dominant frequency, ν_{2*} . Moving these expressions into the t -domain, the following expressions are similarly obtained,

$$x_S(t) \approx \rho_{S*} \cos \theta_2 \quad (39)$$

$$y_S(t) \approx \rho_{S*} \sin \theta_2, \quad (40)$$

where $\theta_2 = -\nu_2 t + \theta_{2,R}$. The frequency with respect to t is computed as $\nu_2 = 0.9234$ n.d., a slightly smaller value as compared to ν_{2*} . This updated value is denoted as the *HFEM synodic* frequency in the current work. The maximum relative errors for x_S and y_S in the t -domain now compute as 10% and 9%, respectively. Not surprisingly, the acceleration from the additional bodies is governed by ν_2 , mainly associated with the in-plane solar location.

For improved insight, it is possible to visualize any reference epoch within the angle domain, (θ_1, θ_2) , as illustrated in Fig. 5. From a sample starting epoch, 09/23/2000, the combination for the two angles (θ_1, θ_2) evolves linearly with t over 25 years. Different colors

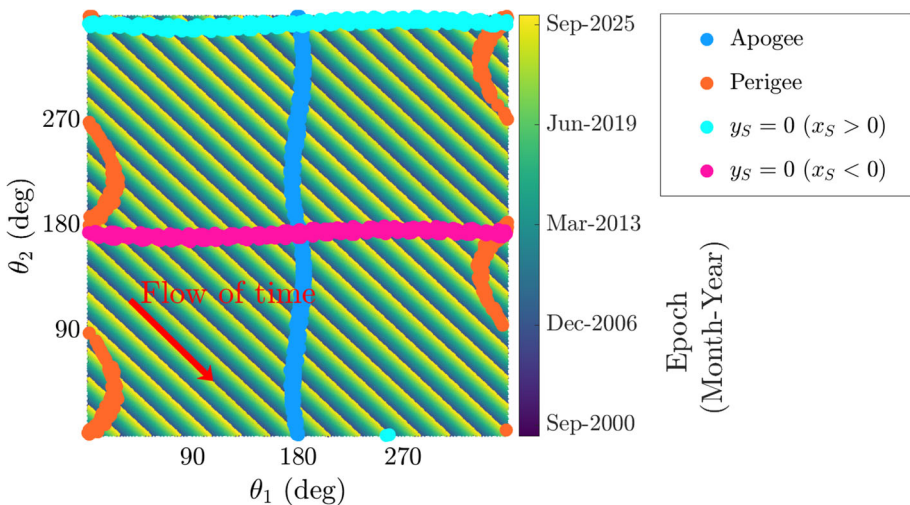


Fig. 5 Angle information over 25 years

denote the associated epoch, where an infinite time is required for the combinations to fill up the two-dimensional space due to the incommensurate frequency ratio. These angles are closely related to the physical quantities that provide some intuition. The first angle, θ_1 , is mainly associated with the Earth–Moon distance. For illustration, epochs when the Moon is located at the apogee are plotted in blue in Fig. 5. These epochs are closely aligned with $\theta_1 \approx 180^\circ$. The epochs when the Moon is located at the perigee are plotted in orange in the sample plot. Note that these epochs exist close to $\theta_1 \approx 0^\circ$, although the perigee timing is much more subject to other frequencies as opposed to apogee epochs. For the second angle, θ_2 , it is straightforward to consider it to be similar to the Sun angle. For illustration, cyan and pink markers are plotted for epochs where $y_S = 0$. While these two angles, i.e., θ_1 and θ_2 , do not exactly correspond to physical quantities, they are closely related to the Earth–Moon distance and the Sun angle, respectively. This visualization leads to an effective reference epoch selection process as discussed in Sect. 4.

3.3 Visualization within the Earth–Moon plane

The relative magnitudes of the accelerations originating from pulsation and additional bodies within the HFEM are illustrated in the $\hat{x} - \hat{y}$ plane, assuming that the s/c position and velocity components are zeros in the \hat{z} direction. From Eq. (20), the in-plane acceleration magnitude from pulsation corresponds to,

$$|\ddot{\rho}_{P,H}| = \sqrt{b_4^2 + (b_5 - 2)^2} \cdot \sqrt{\dot{x}^2 + \dot{y}^2}. \quad (41)$$

The “pulsation coefficient” is then defined as,

$$C_P := \sqrt{b_4^2 + (b_5 - 2)^2} = \sqrt{\frac{l'^2}{4t'^2l^2} + 4\left(\frac{h^2}{t'^2l^4} - \frac{2h}{t'l^2} + 1\right)}, \quad (42)$$

where the magnitude of the acceleration from pulsation is the in-plane *velocity* magnitude multiplied by C_P . Similarly, from Eq. (25), the acceleration magnitude from the additional bodies approximately corresponds to,

$$|\ddot{\rho}_{\mathcal{A},L}| \approx \frac{3\mu_S}{\rho_S^3} |y|. \quad (43)$$

The “solar coefficient” is defined as,

$$C_S := \frac{3\mu_S}{\rho_S^3}, \quad (44)$$

where the magnitude of the acceleration from additional bodies (roughly, the solar gravity) is the y -excursion multiplied by C_S . The relative magnitude of the accelerations is a function of the s/c state in the plane, and the epoch that governs the values for C_P and C_S . A scalar is defined to measure the relative impact of the accelerations from the pulsation and solar gravity as,

$$\gamma := \frac{|\ddot{\rho}_{\mathcal{A},L}| - |\ddot{\rho}_P|}{|\ddot{\rho}_{\mathcal{A},L}| + |\ddot{\rho}_P|} = \frac{\frac{C_S}{C_P} |y| + \sqrt{\dot{x}^2 + \dot{y}^2}}{\frac{C_S}{C_P} |y| + \sqrt{\dot{x}^2 + \dot{y}^2}}, \quad (45)$$

where $\gamma = 1$ implies that the perturbation within the HFEM mainly originates from the solar gravity and $\gamma = -1$ implies that the impact from the pulsation dominates the perturbing acceleration. From the ephemerides, the time histories for C_P and C_S are computed and illustrated in Fig. 6, investigated over 20 years since 09/23/2023. While these quantities display complex behavior as quasi-periodic functions of time, C_P tends to be larger in magnitude than C_S . The maximum and minimum ratios of the coefficients are, $(C_S/C_P)_{max} = 0.97$ and $(C_S/C_P)_{min} = 0.17$, respectively. Thus, given a s/c state, the relative impact between pulsation and solar gravity is bounded between these extremum values. For visualization, it is beneficial to consider the Jacobi constant, or J_C , the integral of motion within the CR3BP defined as,

$$J_C = (x^2 + y^2) + \frac{2(1-\mu)}{\sqrt{(x+\mu)^2 + y^2}} + \frac{2\mu}{\sqrt{(x-1+\mu)^2 + y^2}} - (\dot{x}^2 + \dot{y}^2), \quad (46)$$

for an in-plane motion. Then, for a fixed J_C and C_S/C_P values, γ is computed at different locations within the plane. For illustration, two sample values for J_C are selected as 3.10 and 2.50. Figure 7 illustrates two contour plots for $J_C = 3.10$, where the white areas in the plot correspond to the Hill region, i.e., the s/c cannot access the region for the given J_C value. Figure 7a illustrates a specific epoch when C_S/C_P is minimized, and vice versa for Fig. 7b. Note that the interior region of the system is governed by the pulsation in general. However, the relative impact from the solar gravity becomes non-negligible as the s/c approaches the Hill region and the velocity magnitude decreases. Throughout all the epochs, it is noteworthy that the lunar vicinity is governed by the pulsation, due to the fact that the solar gravity is mainly scaled by the y -excursion of the s/c. Similar plots are generated for a lower J_C value, $J_C = 2.50$, in Fig. 8. Note that the Hill region disappears on the plane for this J_C level. Similar tendencies for γ are observed, where the interior region closer to the primaries is governed by pulsation in general. As L_{4,5} regions are generally characterized by relatively low velocity magnitudes, the relative impact from the solar gravity notably increases.

From these sample J_C values, it is concluded that the vicinities of the primaries, and the regions near the \hat{x} -axis are governed by pulsation, in general. As the focus for a future space mission includes utilization of lunar orbits associated with small y -excursions, e.g.,

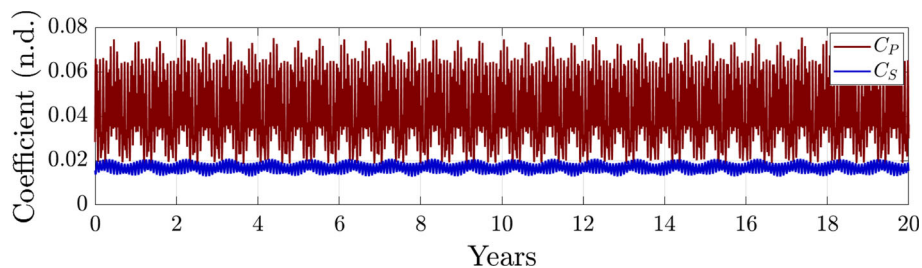


Fig. 6 History of C_P and C_S over 20 years, initial epoch: 09/23/2023

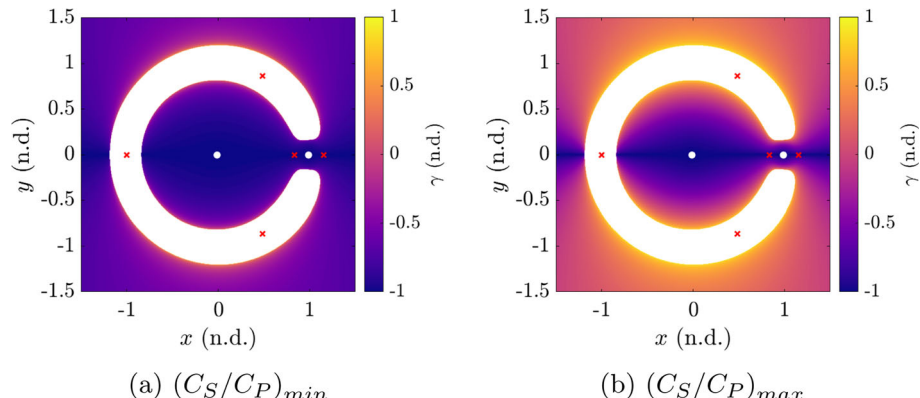


Fig. 7 Contour plot for $J_C = 3.10$

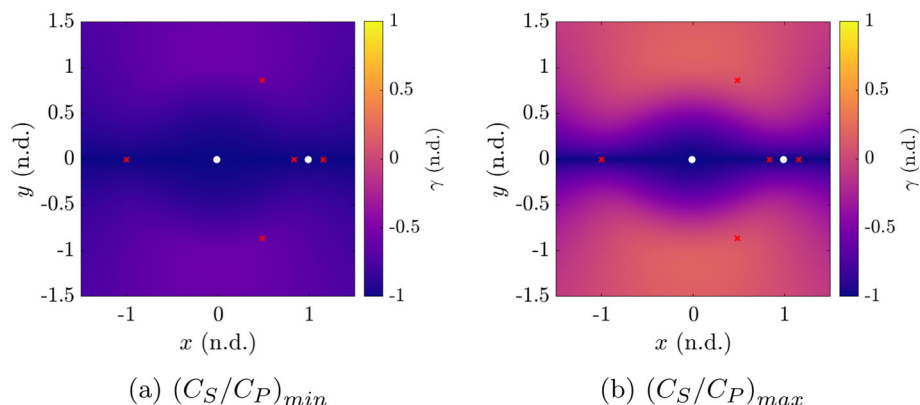


Fig. 8 Contour plot for $J_C = 2.50$

L_2 halo orbits, this information provides valuable insight on the transition process from the CR3BP to the HFEM. Trajectories that stay in the vicinity of $L_{4,5}$ are likely to be influenced heavily by the solar gravity. However, depending on the epoch, pulsation also offers non-negligible perturbations. As the accelerations from pulsation and solar gravity are associated with different dominant frequencies, this visualization technique offers insights into selecting suitable intermediate models that incorporate a single frequency as an enhancement to the

CR3BP. As this analytical approach provides only a “snapshot” of the perturbing accelerations at specific epochs, the insights are further validated by the sample numerical transition process provided in Sect. 5.

4 Evaluation of models

The intermediate models offer more insight into the realistic dynamics as compared to the CR3BP dynamics by incorporating additional perturbing accelerations. The capabilities and limitations of these models within the context of the transition process are illustrated by comparing the corresponding acceleration terms from the HFEM. Note that the HFEM is typically described by multiple frequencies, while the selected intermediate models, i.e., the ER3BP and BCR4BP, incorporate perturbations governed by a single frequency. Thus, the analysis from Sect. 3.2 facilitates the assessment of the value of incorporating the ER3BP and BCR4BP in the transition process. The capabilities of the intermediate models depend on (1) the model parameters and (2) the reference value for the independent variable. The parameters include e for the ER3BP and $\rho_{S,4}$ for the BCR4BP that vary the frequency of the intermediate models as well as the coefficients included in Table 2. As these models are associated with different independent variables as compared to the HFEM, a strategy is required to map the reference independent variables from the intermediate models, i.e., f_R and $\theta_{S,4,R}$, to the reference epoch within the HFEM, JD_R . This mapping is also termed *epoch initialization* here, and several schemes are explored in previous literature (Boudad et al. 2022; Peng and Bai 2018) for the intermediate models. Performance of these models as a function of these parameters as well as the epoch initialization schemes is assessed.

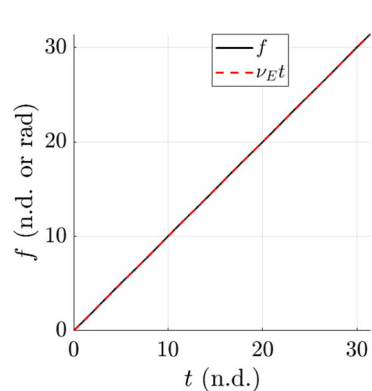
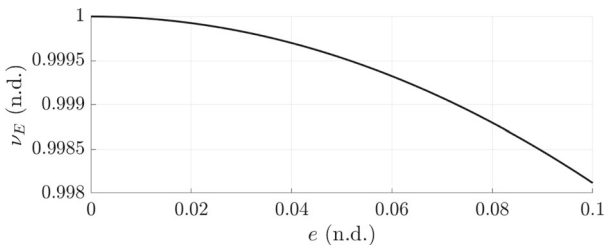
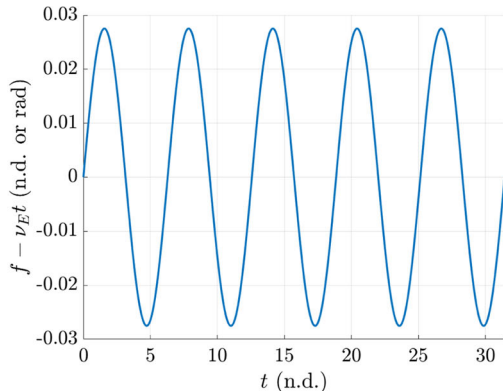
4.1 Assessment of the ER3BP

The capabilities and limitations of the ER3BP to serve as an intermediate frame are assessed in terms of $\ddot{\rho}_P$. Note that as additional bodies are not included in the ER3BP, i.e., $\mathcal{A} = \emptyset$, the ER3BP only provides a zero estimate for $\ddot{\rho}_{\mathcal{A}}$. Then, the ER3BP is assessed in terms of $b_{4,5,12a}$, as these coefficients constitute the acceleration from pulsation, i.e., $\ddot{\rho}_P$. While these terms are comprised of several time-varying quantities in the HFEM governed by multiple frequencies, the ER3BP incorporates one frequency. Thus, the capabilities and limitations of the ER3BP depend on the approach to approximate these non-periodic quantities originating from $\ddot{\rho}_{P,H}$ with only one frequency.

Initially, the frequency of the ER3BP in the t -domain is investigated and compared with the HFEM analysis where $v_1 = 0.9896$ n.d. arises as the dominant frequency for $\ddot{\rho}_{P,H}$. The ER3BP dynamics is periodic with respect to the true anomaly, where the period is 2π radians in true anomaly. Note that the coefficients $b_{4,5,12a}$ are also periodic functions with respect to f as apparent in Table 2; the frequency of the ER3BP in the f -domain is unity. However, in the t -domain, the frequency is a function of e , as t and f are related via a differential equation as described in Eq. (18). The period in the ER3BP is computed as,

$$t_E = \int_0^{2\pi} \frac{1}{\sqrt{1 + e \cos f}} df, \quad (47)$$

where the frequency of the ER3BP renders $v_E = 2\pi/t_E$ in the t -domain. This expression involves an elliptic integral, where numerical evaluation of v_E as a function of e is provided in Fig. 9. Note that $v_E < 1$ for $e > 0$, but the frequency remains near unity for the realistic

Fig. 9 ν_E as a function of e (a) f and $\nu_E t$ (b) $f - \nu_E t$ **Fig. 10** Approximation of $f \approx \nu_E t$

eccentricity values for the Earth–Moon system; the osculating eccentricity for the lunar orbit around the Earth is approximately bounded between 0.035 and 0.091 across all epochs.

While a simple analytical relationship does not exist between t and f , to facilitate analysis, it is initially approximated as $f \approx \theta_E$, where the phase angle θ_E is defined as a linear function of t as $\theta_E = \nu_E t + \theta_{E,R}$; then, the reference value for the true anomaly for epoch initialization is $f_R = \theta_{E,R}$. This approximation is more accurate for smaller values for e . For a sample value for $e = 0.055$ that results in $\nu_E \approx 0.9994$, f and $\nu_E t$ are plotted together in Fig. 10a, where both functions are closely aligned. The isochronous difference between these expressions is illustrated in Fig. 10b, where the deviation remains bounded to an oscillatory behavior with a relatively small amplitude. Thus, it is reasonable to initially consider $f \approx \theta_E$ for an efficient characterization of the ER3BP coefficients in the t -domain. For a full representation, f is a summation of the linear function $\nu_E t$ and a series of trigonometric functions that represent the oscillatory behavior, where the frequency for each term is a multiple of ν_E . Here, it is sufficient to consider the linear part to assess the closeness of the ER3BP coefficients as compared to those from the HFEM.

Under this formulation, the coefficients $b_{4,5,12a}$ for the ER3BP are approximated as,

$$b_{4,E} = -\frac{e \sin f}{2\sqrt{1+e \cos f}} \approx -\frac{e}{2} \sin \theta_E \quad (48)$$

$$b_{5,E} = 2\sqrt{1+e \cos f} \approx 2 + e \cos \theta_E \quad (49)$$

$$b_{12a,E} = -e \cos f \approx -e \cos \theta_E, \quad (50)$$

where linear approximations $1/\sqrt{1+e\cos f} \approx 1 - e\cos f/2$ and $\sqrt{1+e\cos f} \approx 1 + e\cos f/2$ are leveraged and terms that contain e^2 are ignored. While exact evaluation of these coefficients requires integration of Eq. (18), Eqs. (48)–(50) are sufficient to capture some important qualitative behavior. First, v_E arises as the dominant frequency in the ER3BP. This frequency is denoted as the *ER3BP pulsation* frequency in the current investigation. This frequency is also denoted as the *ER3BP sidereal* frequency, as pulsation and sidereal frequencies are identical for the ER3BP that assumes a conic orbit for the Moon relative to Earth. Recall that the approximate functions from the HFEM are associated with the frequency $v_1 = 0.9896$ in the t -domain from Eqs. (33)–(35). Thus, an innate discrepancy between the ER3BP pulsation frequency and the HFEM pulsation frequency exists, as $v_E \approx 1$ for $e > 0$. Note that $v_1 < 1$ in the HFEM, as the lunar perigee gradually processes due to the solar gravity. This information is not incorporated in the ER3BP, resulting in the slight mismatch between the frequencies. However, the similarity between the expressions from Eqs. (33)–(35) and Eqs. (48)–(50) is noticeable. Investigating the values for $b_{4,1}$, $b_{5,1}$ and $b_{12a,1}$ in Table 4, it is deduced that e values between 0.05 and 0.055 are generally desired as it produces similar coefficients corresponding to the pulsation acceleration over time. For the current analysis, $e = 0.055$ is utilized as a sample value, but the ER3BPs constructed with nearby values are also expected to provide similar benefits as they closely follow the corresponding HFEM coefficients. For reference, $e = 0.0554$ is successfully leveraged by Peng and Bai (2018).

A proper epoch initialization scheme for the ER3BP involves a mapping between reference values for the dimensional epoch, JD_R , and the true anomaly, f_R . From the comparison of the expressions between Eqs. (33)–(35) and Eqs. (48)–(50), it is intuitive to consider $\theta_{1,R} = \theta_{E,R}$, and a desirable value for f_R is initialized as $f_R = \theta_{E,R}$. Despite the innate difference in the frequencies between the HFEM and ER3BP, utilizing a consistent reference angle for θ_1 and θ_E is likely to minimize the deviations in the coefficients for a fixed span of time relative to the reference epoch. To illustrate this behavior, one of the coefficients, b_4 , is plotted in Fig. 11 following this initialization scheme ($f_R = \theta_{E,R} = \theta_{1,R}$). The black curve corresponds to $b_{4,H}$, constructed from the ephemerides. While it is noted that the curve displays complex behavior with multiple frequencies, the most dominant oscillatory term is associated with v_1 . Here, $t = 0$ corresponds to a sample initial epoch retrieved from Fig. 5 where $\theta_{1,R} \approx 306^\circ$, corresponding to 09/23/2023. Then, utilizing the same value, the ER3BP is properly initialized with $f_R = \theta_{1,R}$. The corresponding coefficient, $b_{4,E}$, is generated from the expression in Table 2 along with Eq. (18). It is noted that in the vicinity the reference epoch, the peaks and troughs of both plots are nearly synchronized, a property that is achieved by synchronizing the reference phase angle for $\theta_{1,R} = \theta_{E,R}$. The isochronous difference between the coefficients for these models is illustrated in Fig. 12. It is observed, not surprisingly, that the epoch initialization scheme $\theta_{1,R} = \theta_{E,R} = f_R$ tends to reduce the error between the models in the vicinity of the reference epoch, a straightforward conclusion from the formulation of the trigonometric expressions. As this desired epoch initialization scheme requires a computation of $\theta_{1,R}$, constructed from the ephemerides over a sufficiently long time span, the apsis timings provide a relatively simple alternative epoch initialization scheme. In Fig. 5, note that the epochs where $\theta_1 = 180^\circ$ are closely aligned with the apogee epochs; for the epochs when the Earth–Moon distance is locally maximized, it is possible to leverage $\theta_{1,R} \approx f_R = 180^\circ$ as an approximation of the “optimal” reference true anomaly value. However, a similar strategy is less reliable for the perigee epochs, as the perigee timings are more subject to the other frequencies as apparent from Fig. 5.

The ER3BP provides a better estimate for the perturbing acceleration caused by pulsation compared to the CR3BP over a 1-year span, as demonstrated in Fig. 12. However, there

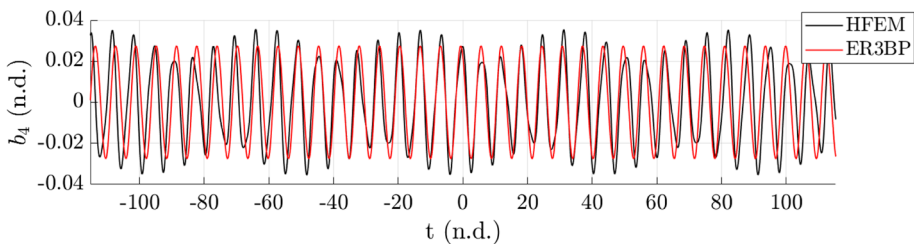


Fig. 11 b_4 comparison between the HFEM and ER3BP

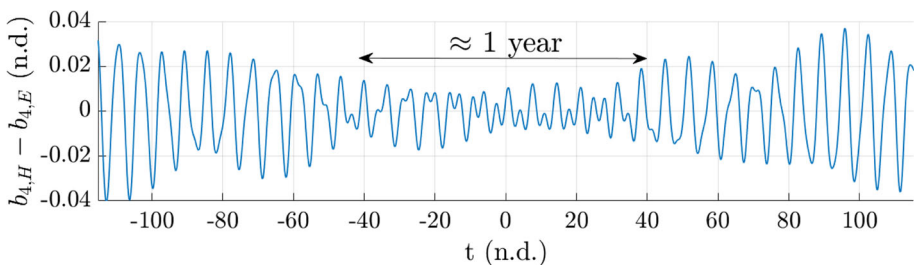


Fig. 12 b_4 difference between the HFEM and ER3BP

Table 5 Assessment of the ER3BP within the context of transition

	HFEM pulsation	ER3BP pulsation
Acceleration expression	$\ddot{\rho}_{P,H}$	$\ddot{\rho}_{P,E}$
Dominant frequency (t -domain)	$\nu_1 \approx 0.9896$	$\nu_E \approx 0.9994$ ($e = 0.055$)
Epoch initialization scheme	$f_R = \theta_{1,R}$	<ul style="list-style-type: none"> – Close estimates on the pulsation acceleration – Gradual degradation due to difference in ν
	Capabilities and limitations	

exists a natural discrepancy between the HFEM pulsation frequency (ν_1) and the ER3BP pulsation frequency (ν_E) that causes the ER3BP coefficient functions to gradually misalign with those of the HFEM. This deviation reflects the fact that the conic motion of the Moon within the ER3BP eventually becomes out-of-sync with the realistic lunar motion for the HFEM. Although Figs. 11 and 12 describe b_4 as an example, the same behavior is observed for other coefficients, b_5 and b_{12a} .

Still, the ER3BP is expected to provide useful insights on the evolution of the CR3BP solutions under the additional accelerations originating from pulsation; the relevant information is summarized in Table 5. More discussions are provided in the context of a numerical transition procedure in Sect. 5 that leverages the ER3BP structure as an enhanced initial guess.

4.2 Assessment of the BCR4BP

Similar to the ER3BP evaluation, the capabilities and limitations of the BCR4BP as an intermediate model are assessed in terms of the acceleration from the additional bodies, i.e., $\ddot{\rho}_{\mathcal{A}}$. For the BCR4BP, the acceleration is evaluated as,

$$\ddot{\rho}_{\mathcal{A},4} = -\frac{\mu_S}{\rho_{S,4}^3} \vec{\rho}_{S,4} - \frac{\mu_S}{\rho_{Sc}^3} \vec{\rho}_{Sc}, \quad (51)$$

where subscript ‘4’ denotes the BCR4BP. The first term corresponds to the gravitational influence of the Sun on B , and the second term denotes the direct influence of the Sun on the s/c. The solar position remains in plane and is represented as $\vec{\rho}_{S,4} = \rho_{S,4} \cos \theta_{S,4} \hat{x} + \rho_{S,4} \sin \theta_{S,4} \hat{y}$. The model parameter for the BCR4BP is $\rho_{S,4}$ that changes the frequency of the model as $v_4 = (1 - n_S)$, where it is recalled that $n_S = \sqrt{\frac{\tilde{\mu}_S + \tilde{\mu}_E + \tilde{\mu}_M}{(\tilde{\mu}_E + \tilde{\mu}_M)\rho_{S,4}^3}}$. Here, v_4 corresponds to the *BCR4BP synodic* frequency. Different BCR4BPs associated with adjusted frequencies may be constructed for various analyses (Boudad 2022). However, regardless of the choice for these parameters, in general, the BCR4BP does not accurately estimate the $\ddot{\rho}_{\mathcal{A}}$ from the HFEM in the pulsating–rotating frame. For illustration, consider the contour plots in Fig. 13, where $\ddot{\rho}_{\mathcal{A}}$ is compared between the BCR4BP and HFEM; the instantaneous values $\theta_{S,4} \approx -105^\circ$, $\rho_{S,4} \approx 389$ n.d., $n_S \approx 0.0748$ n.d. are employed to construct the BCR4BP. Note that $\rho_{S,4} = \rho_{S,*}$, or, the mean quantity from the HFEM (Eq. (36)) is utilized as a suitable value. Under this definition, the BCR4BP synodic frequency is $v_4 \approx 0.9252$ n.d., a slightly larger value as compared to the HFEM synodic frequency, $v_2 \approx 0.9234$ n.d. Regardless of these values, however, the contour plots for the BCR4BP and HFEM display noticeably different patterns. While the magnitude of $\ddot{\rho}_{\mathcal{A},4}$ gradually increases in the radial direction from B , the magnitude of $\ddot{\rho}_{\mathcal{A},H}$ is mainly dependent on the y -excursion. As a result, the difference between the accelerations from the two models results in non-negligible magnitudes across cislunar space. This tendency holds for all epochs, where the concentric circle patterns in the third plot only slightly rotate and pulsate depending on the selected epoch. This difference originates from the fact that the BCR4BP is not constructed in a coherent manner. For the HFEM, expressions for b_{1-3} are partly cancelled by b_{7-12} , resulting in the linear relationship described in Eq. (24). However, while the BCR4BP incorporates some solar perturbations in the form of coefficients b_{1-3} , it only provides constant values for b_{7-12} that do not cancel b_{1-3} . Thus, the challenge in the use of the BCR4BP as an intermediate model is apparent. It does not completely bridge the gap between the coefficients for the CR3BP and HFEM, and it does not always characterize the dynamics adequately within the pulsating–rotating frame across the entire cislunar space. When the BCR4BP supplies a unique solution that deviates from the original CR3BP solution within the pulsating–rotating frame, the geometry change is driven by $\ddot{\rho}_{\mathcal{A},4}$ that, generally, is an inadequate approximation for $\ddot{\rho}_{\mathcal{A},H}$ in the interior region.

For the BCR4BP epoch initialization, it is desired that the relative geometry in the Sun–Earth–Moon system is maintained across the BCR4BP and the HFEM. Boudad et al. (2022) note that such a configuration is satisfied for $\theta_{S,R} = \theta_{S,4,R}$, where the subscript R denotes the reference values. In the current work, $\theta_{2,R} = \theta_{S,4,R}$ is leveraged alternatively to be consistent with the frequency analysis in Sect. 3.2. However, both schemes produce similar results as apparent from Fig. 5 since $\theta_S \approx \theta_2$. The analysis of the BCR4BP in the context of transition is summarized in Table 6.

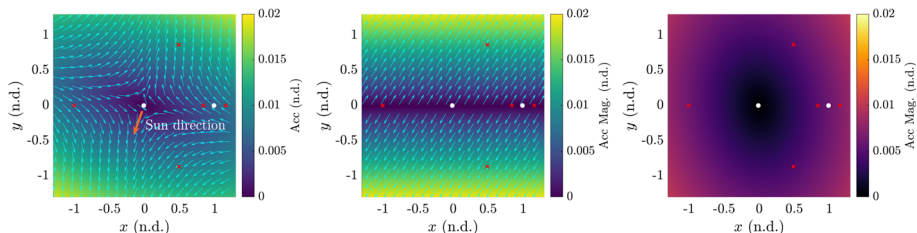


Fig. 13 Contour plots for $\ddot{\rho}_{\mathcal{A},4}$ (left), $\ddot{\rho}_{\mathcal{A},H}$ (center), and $\ddot{\rho}_{\mathcal{A},H} - \ddot{\rho}_{\mathcal{A},4}$ (right), epoch: 09/23/2023

Table 6 Assessment of the BCR4BP in the context of transition

	HFEM solar gravity	BCR4BP solar gravity
Acceleration expression	$\ddot{\rho}_{\mathcal{A},H}$	$\ddot{\rho}_{\mathcal{A},4}$
Dominant frequency (t -domain)	$v_1 \approx 0.9234$	$v_4 \approx 0.9252 (\rho_{S,4} \approx 389)$
Epoch initialization scheme	$\theta_{S,4,R} = \theta_{2,R}$	
Capabilities and limitations	– Coherence issue → fundamental limitation	

5 Application: transitioning L₂ halo orbits

While the investigation of the coefficients for the EOMs offers useful insight regarding the additional perturbations in the HFEM and the capabilities of the ER3BP and BCR4BP, it requires further validation. As noted previously, the small relative values of the coefficients and the associated accelerations do not necessarily guarantee that the solutions from the intermediate models are better preserved in the HFEM. Also, the comparison of the coefficients requires an isochronous correspondence definition, potentially a limiting assumption in any actual transition from a lower-fidelity model to the HFEM. Typically, the independent variables, or times, are incorporated as parts of the initial guess for the transition process; subsequently, the time variables are also under adjustments. Thus, for further validation, a sample transition problem is introduced, where a ballistic CR3BP orbit is transitioned into the HFEM.

For demonstration, the L₂ southern halo orbit family serves as the basis for the sample scenario. The first plot in Fig. 14 displays several CR3BP periodic orbits in the family within the pulsating–rotating frame, colored differently according to the period of the orbits. When transitioned to the HFEM, the periodicity of the original solution is no longer guaranteed. To preserve the geometry of the original periodic orbits, one common practice is to stack multiple revolutions of the orbits and enforce continuity along the trajectory, utilizing a multiple shooting algorithm (Davis et al. 2017). This strategy locates possible structures within the HFEM in the vicinity of the stack of orbits; a minimum-norm solution is typically employed to locate suitable arcs that are geometrically very similar without explicitly incorporating an optimizer. Utilizing such techniques, sample analog trajectories over 1 year in the HFEM are produced by directly transitioning the selected L₂ halo orbits from the CR3BP, as illustrated in the second plot of Fig. 14. For fast computation, only the Sun is incorporated as the additional body in the HFEM. Noted by previous authors (Davis et al. 2017; Boudad et al. 2022), some members of the family in a particular region evolve into solutions that deviate significantly from the original CR3BP solutions when transitioned to the HFEM in comparison with the majority of the members of the family. While this *challenging region* is not well-bounded,

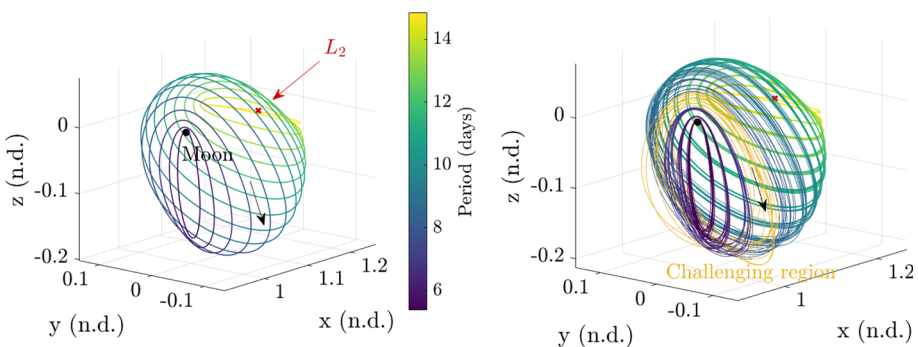


Fig. 14 L₂ halo orbits in the CR3BP (left), transitioned results in the HFEM (right), viewed in the pulsating–rotating frame

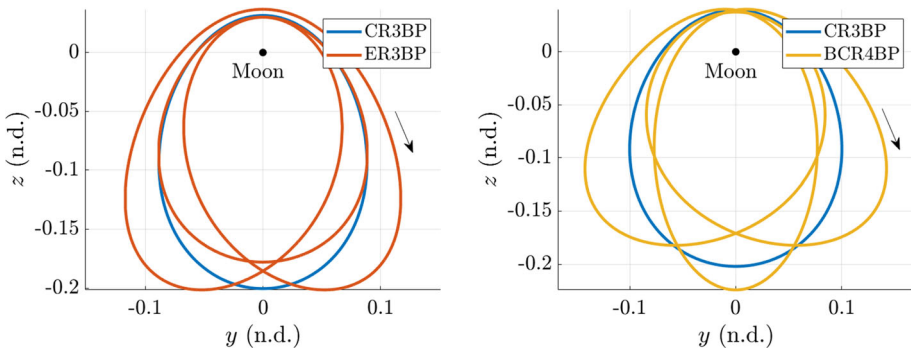


Fig. 15 Sample orbits: 3:1 sidereal (left) and 3:1 synodic (right), viewed in the pulsating–rotating frame

orbits with periods ranging between 9 and 10 days tend to converge to solutions with behavior in the HFEM that appears more random. This region serves as a suitable test case for the current analysis, as the HFEM perturbations notably impact the CR3BP structures and the CR3BP alone, e.g., bifurcation analysis (Boudad et al. 2022), provides only limited clarity for the behavior. Based on the contour plot in Fig. 7, it is evident that the regions with small y -excursions are under more influence from the pulsation as opposed to the solar gravity. Maximum y -excursions for L₂ halo orbits are less than 0.15 n.d., considered sufficiently small from the contour plot. Hence, the analysis in previous sections suggests that the ER3BP is likely to provide useful insight.

To verify this insight concerning the challenging region, sample orbits in the CR3BP and the corresponding counterparts are computed within the intermediate models. Two CR3BP halo orbits are plotted in Fig. 15, where the periods of the orbits approximately correspond to 9.1 and 9.8 days. As these periods are exactly one third of the ER3BP pulsation (sidereal) and BCR4BP synodic periods, the CR3BP halos are denoted as the 3:1 sidereal halo and 3:1 synodic halo, respectively. The counterpart periodic orbits within the ER3BP and BCR4BP are then produced via continuation in e and μ_S (Ferrari and Lavagna 2018; Boudad et al. 2020). The resulting counterpart orbits consist of three distinct lobes around the Moon as displayed in Fig. 15. Since the intermediate models are time-dependent systems, the periodic solutions are associated with specific epoch conditions. For the ER3BP orbit corresponding to the 3:1 sidereal halo, the timing of the apolune in the middle lobe coincides with $f = 180^\circ$.

For the BCR4BP orbit originating from the 3:1 synodic halo, the timing of the apolune in the middle lobe coincides with $\theta_{S,4} = 0^\circ$. For the selection of a reference epoch within the HFEM, $\theta_1 = 180^\circ$ and $\theta_2 = 0^\circ$ serve as adequate approximations, following the epoch initialization schemes outlined in Tables 5 and 6.

Next, two transition cases are compared: (1) direct transition, where CR3BP halo is directly transitioned into the HFEM, and (2) utilization of periodic orbits within the intermediate models as evolving initial guess for the transition. To ensure consistency in the analysis, the following parameters are commonly adopted in the multiple shooting algorithm for the CR3BP halos: 12 revolutions of the orbit are stacked starting from the apolune state, each revolution consists of five segments that are equally divided in t , and the reference (baseline) epoch is fixed to correspond to the apolune of the innermost (7th) revolution. When transitioning the ER3BP and BCR4BP periodic orbits, only 4 revolutions of the orbit are stacked since each revolution in the intermediate models corresponds to three revolutions of the original CR3BP orbit. This consistent formulation is utilized for both (1) the direct transition and (2) the transition leveraging intermediate models for a proper comparison. While different sets of parameters may result in slightly varying results, this aspect remains beyond the scope of the present investigation; the current set of parameters is representative of sample values. For the shooting algorithm, a Newton–Raphson method is leveraged, where the free variable vector, \vec{X} , that contains the position, velocity, and epoch components at patchpoints between the segments, is updated at the i -th step as,

$$\vec{X}_{i+1} = \vec{X}_i - \alpha \cdot \mathbf{J}^\top (\mathbf{J} \mathbf{J}^\top)^{-1} \vec{F}, \quad (52)$$

where \vec{F} is the constraint vector that consists of continuity constraints in both the epoch and the state across all segments. The Jacobian matrix of \vec{F} with respect to \vec{X} is denoted as \mathbf{J} , and $0 < \alpha \leq 1$ corresponds to an attenuation factor. The iteration is repeated until the nondimensional magnitude of \vec{F} is reduced to a value below 10^{-10} , defined as *convergence*. Note that the dimension of \vec{X} is typically larger than that of \vec{F} for the HFEM transition process (Dei Tos and Topputo 2017b), and this formulation corresponds to a minimum-norm approach to define the search direction for the underconstrained problem. The transition cases between the CR3BP and intermediate models leverage the same reference epoch for comparison. For the ER3BP periodic orbit, epochs where $\theta_1 = 180^\circ$ are leveraged as the reference value, and the same epochs are incorporated for the direct transition. Multiple epochs satisfy this condition, and 300 different epochs starting from 01/01/2000 are selected that are all associated with $\theta_1 = 180^\circ$ but with various θ_2 values. Testing these multiple epochs clarifies the dominant frequency, i.e., comparing the impact of θ_1 and θ_2 on the transition behavior. For the BCR4BP, similarly, 300 different epochs that corresponds to $\theta_2 = 0^\circ$ are initially selected for the reference epochs. The goal is to determine whether the intermediate models provide an enhanced initial guess in the transition process to result in a smoother transition; the number of steps in the Newton–Raphson method before convergence is leveraged to assess the nearness of the initial guess to the converged basin. The relevant model parameters are included in Table 7. Note that approximate values are listed except for $e = 0.055$. The initial conditions for the periodic orbits in Fig. 15 are provided in Tables 8 and 9, where the subscript R represents the reference state at the initial epoch.

5.1 ER3BP results

The transition results employing the ER3BP are provided in Fig. 16a in comparison to the CR3BP, where x -axis represents the θ_2 values that correspond to different epochs while

Table 7 Model parameters

Parameter	Value	Applicable models
μ (n.d.)	0.0121506	CR3BP, ER3BP, BCR4BP
e (n.d.)	0.055	ER3BP
μ_S (n.d.)	3.2890056×10^5	BCR4BP
n_S (n.d.)	0.0748013	BCR4BP

Table 8 Initial conditions for the sample sidereal resonant orbits in Fig. 15

	CR3BP	ER3BP
x_R (n.d.)	1.0637859	1.0612434
y_R (n.d.)	0	0
z_R (n.d.)	-0.2004015	-0.1778929
\dot{x}_R or $(dx/df)_R$ (n.d.)	0	0
\dot{y}_R or $(dy/df)_R$ (n.d.)	-0.1776102	-0.2068254
\dot{z}_R or $(dz/df)_R$ (n.d.)	0	0
Period (n.d.)	$2\pi/3$	2π
Reference epoch	N/A	$f_R = 180^\circ$

Table 9 Initial conditions for the sample synodic resonant orbits in Fig. 15

	CR3BP	BCR4BP
x_R (n.d.)	1.0750359	1.0524406
y_R (n.d.)	0	0
z_R (n.d.)	-0.2021298	-0.2242797
\dot{x}_R (n.d.)	0	0
\dot{y}_R (n.d.)	-0.1921894	-0.1281807
\dot{z}_R (n.d.)	0	0
Period (n.d.)	$2\pi/(3 \cdot (1 - n_S)) \approx 2.2637247$	$2\pi/(1 - n_S) \approx 6.7911741$
Reference epoch	N/A	$\theta_{S,4,R} = 0^\circ$

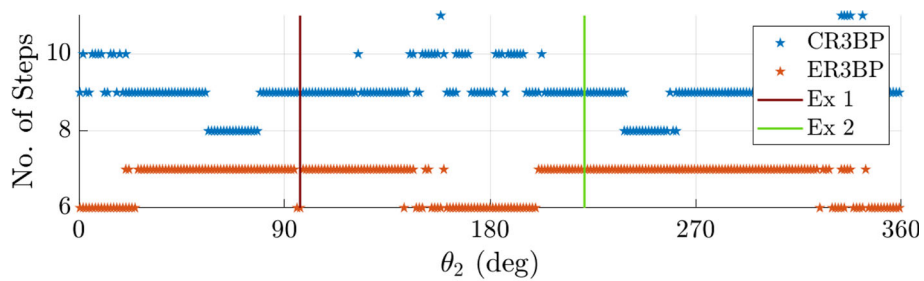
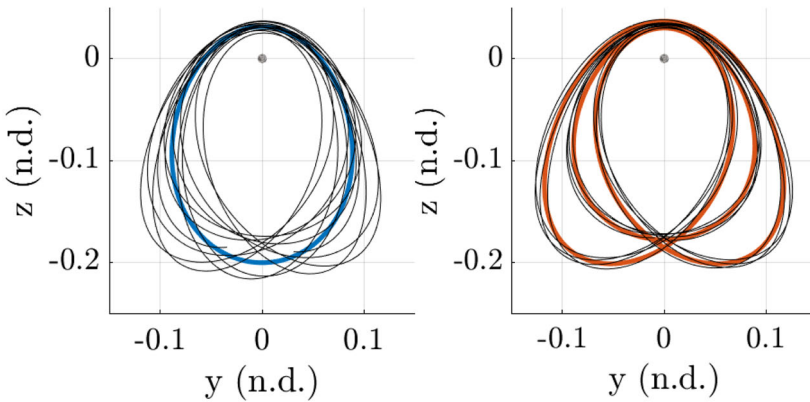
θ_1 is fixed at 180° as required by the ER3BP. An attenuation factor is set to $\alpha = 1$ for both the CR3BP and ER3BP. The label “CR3BP” corresponds to the results obtained via a direct transition process where the CR3BP periodic orbit is stacked as the initial guess. The “ER3BP” cases leverage the ER3BP 3:1 sidereal periodic orbit that originates from the identical CR3BP orbit as illustrated in Fig. 15; the ER3BP orbit is then stacked as an enhanced initial guess for the transition. Regardless of the θ_2 values, the ER3BP provides a smoother transition process as opposed to the CR3BP, apparent from the fact that the ER3BP requires consistently smaller numbers for Newton–Raphson iterations. Thus, for this particular orbit, it is confirmed that the transition results are mainly dependent on θ_1 , associated with the pulsation frequency, as compared to θ_2 that is related to the synodic frequency; the ER3BP periodic orbit supplies an enhanced initial guess in terms of the solution geometry and the reference transition epoch. Two sample epochs are selected to describe the resulting geometries from the transition process in Fig. 16b and c, corresponding to two vertical lines in Fig. 16a. Visually, the solutions transitioned from the ER3BP are more tightly converged around the initial guess from the ER3BP as opposed to the CR3BP case. For the sample cases,

the error from violating the continuity constraint (\vec{F}) monotonically decreases for the ER3BP, whereas the CR3BP requires a few initial iterations before the corrector locates a basin of attraction, explaining the difference in the required numbers of iterations. It is noted that the ER3BP offers some systematic understanding of the evolution of the CR3BP structures under pulsation. The ER3BP periodic orbit is associated with a three-lobe geometry that accurately approximates the evolution of the original CR3BP periodic orbit into the HFEM. Thus, even when the ER3BP solutions are not directly leveraged as an enhanced initial guess for the HFEM transition, they do offer insight into the potential geometry changes under pulsation; the CR3BP alone provides only limited clarity for the appearance of the three-lobe geometry in this region. This challenge from the CR3BP is often mitigated with extra computational efforts. The ER3BP, as an intermediate model, offers more informed predictions regarding the reference epoch, as the ER3BP structures are associated with particular values for the true anomaly that narrow the search space for the favorable reference epoch. For the current orbit, it is demonstrated that reference epochs associated with $\theta_1 = 180^\circ$ serve as suitable reference epochs. Of course, it is emphasized that these benefits are valid for this sample region, and the results cannot be generalized to other regions across cislunar space, especially when the y -excursion of the s/c is non-negligible. While the ER3BP aids in the HFEM transition process for this sample orbit, the capabilities and limitations must be further verified in other regions in cislunar space.

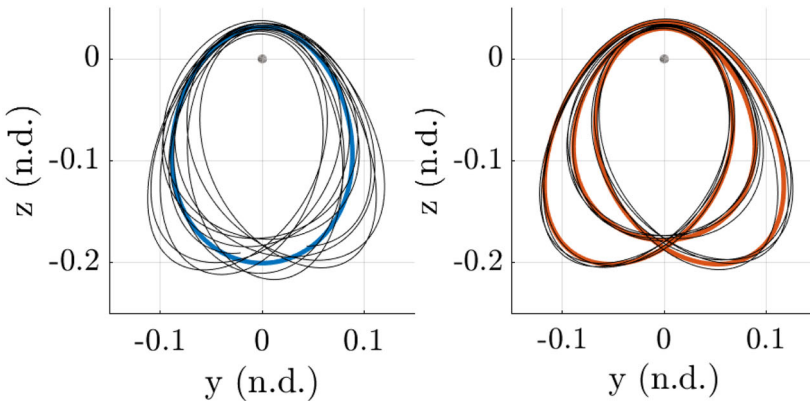
5.2 BCR4BP results

The results for the BCR4BP are included in Fig. 17. The labels “CR3BP” and “BCR4BP” correspond to transition processes that leverage the CR3BP periodic orbit directly and the BCR4BP 3:1 synodic periodic orbit as an enhanced initial guess, respectively, from Fig. 15. An attenuation factor of $\alpha = 0.5$ is leveraged and the maximum number of iterations is capped at 100 for both the CR3BP and BCR4BP cases, as the transition process typically departs from the initial guess for this orbit otherwise. The x -axis of the plot corresponds to different θ_1 angles while fixing $\theta_2 = 0^\circ$ as required by the BCR4BP. As expected, the BCR4BP does not provide consistent benefits in comparison with the CR3BP when utilized as the only intermediate model for this particular application. For many reference epochs, the initial guess from the BCR4BP requires more iterations, or even fails to converge for a given maximum number of iterations. Thus, in general, the BCR4BP does not provide consistent information that is applicable to the transition process in this given region. It is evident, however, that the BCR4BP still converges in a smoother manner for $\theta_1 \approx 0$, again confirming that the perturbations are governed by pulsation, characterized by the dominant frequency θ_1 , not θ_2 .

To confirm this information, another set of transition epochs are considered, where $\theta_1 = 0^\circ$ is selected to transition the BCR4BP solution. This process is considered *inconsistent*, as the geometry of the BCR4BP is leveraged but the epoch information from the BCR4BP is selectively ignored and substituted with θ_1 that is not modeled in the BCR4BP. The results in Fig. 18 indicate that the BCR4BP produces a better initial guess for the transition process. The attenuation factor is $\alpha = 1$, as $\theta_1 = 0^\circ$ now serves as a proper reference epoch and the transition process displays smoother behavior in general. In this case, regardless of the θ_2 angle, it is noted that the BCR4BP initial guess converges with less steps in the correction process as compared to the CR3BP. This result likely originates from underlying dynamical structures mainly governed by θ_1 , where the BCR4BP *happens* to locally supply similar geometry in position space.

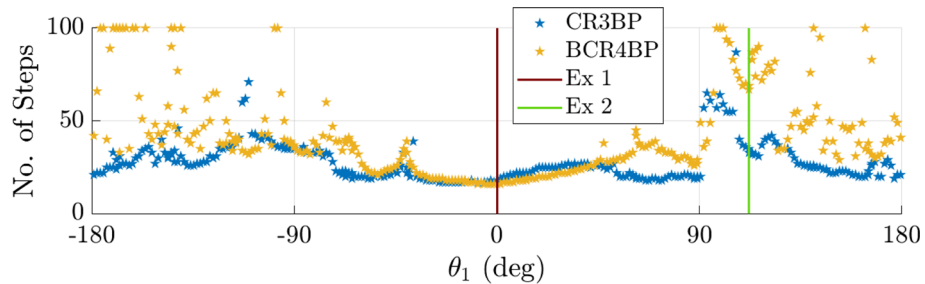
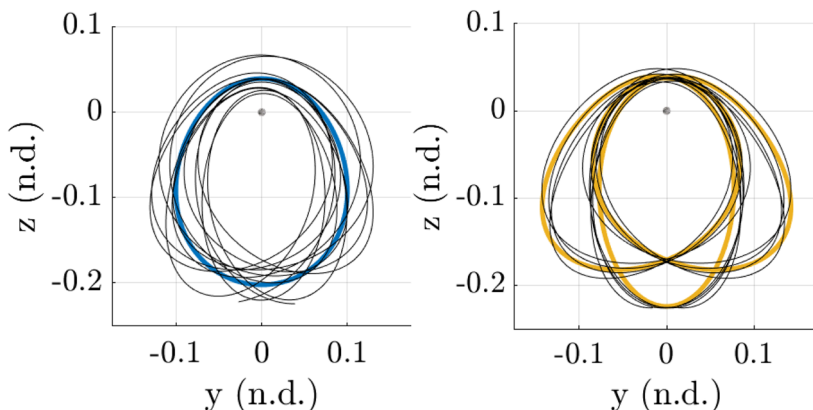
(a) CR3BP vs. ER3BP transition results for $\theta_1 = 180^\circ$ 

(b) Example epoch 1 (08/19/2003): CR3BP (left) and ER3BP (right)

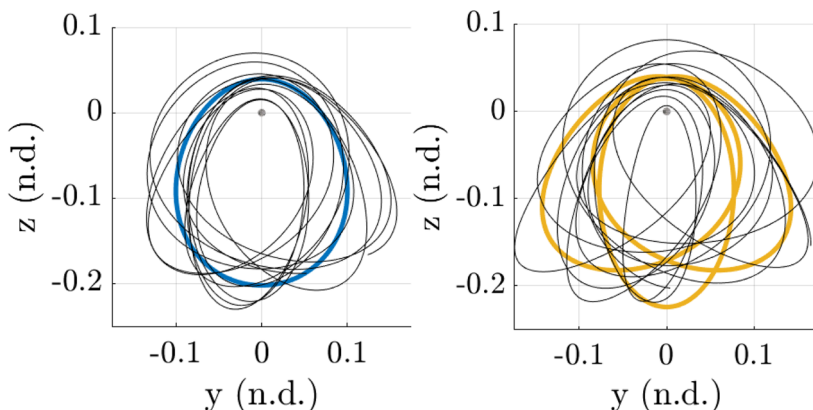


(c) Example epoch 2 (05/28/2007): CR3BP (left) and ER3BP (right)

Fig. 16 Comparing the CR3BP and ER3BP transition results for the 3:1 sidereal halo, $\theta_1 = 180^\circ$, viewed in the pulsating-rotating frame

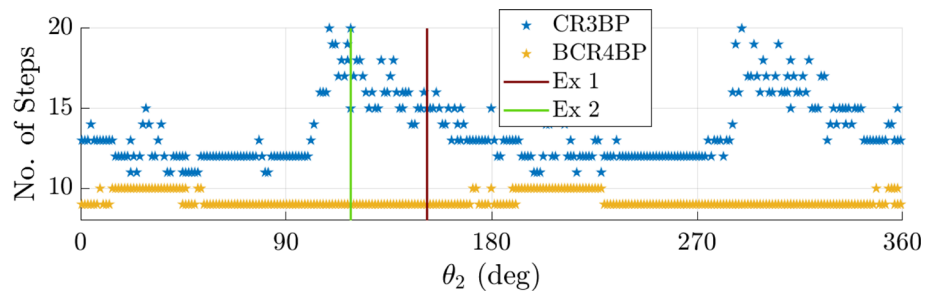
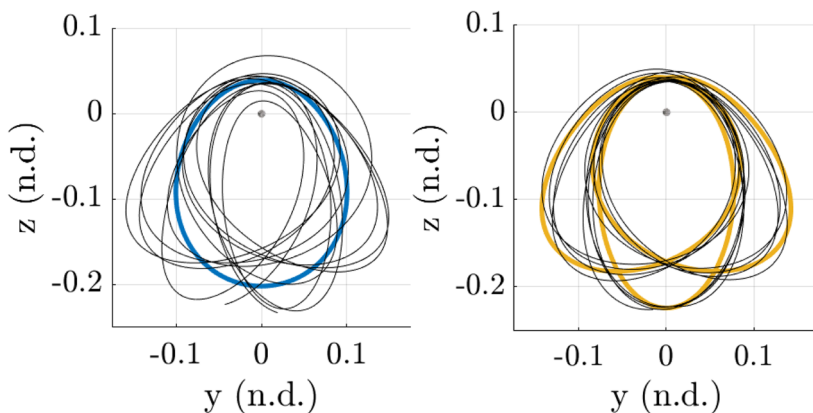
(a) CR3BP vs. BCR4BP transition results for $\theta_2 = 0^\circ$ 

(b) Example epoch 1 (04/14/2017): CR3BP (left) and BCR4BP (right)

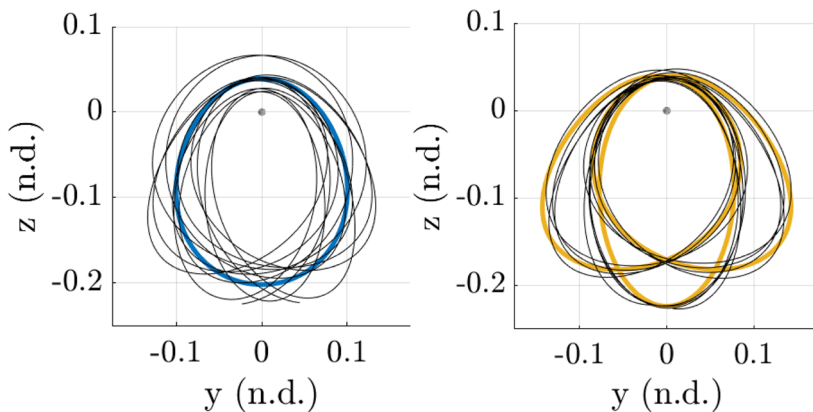


(c) Example epoch 2 (01/30/2012): CR3BP (left) and BCR4BP (right)

Fig. 17 Comparing the CR3BP and BCR4BP transition results for the 3:1 synodic halo, $\theta_2 = 0^\circ$, viewed in the pulsating-rotating frame

(a) BCR4BP vs. CR3BP transition results for $\theta_1 = 0^\circ$ 

(b) Example epoch 1 (11/08/2011): CR3BP (left) and BCR4BP (right)



(c) Example epoch 2 (04/22/2012): CR3BP (left) and BCR4BP (right)

Fig. 18 Comparing the BCR4BP and CR3BP transition results for the 3:1 synodic halo, $\theta_1 = 0^\circ$, viewed in the pulsating-rotating frame

6 Concluding remarks

Various dynamical models are assessed within the context of transitioning from the Earth–Moon Circular Restricted Three-Body Problem (CR3BP) to a Higher-Fidelity Ephemeris Model (HFEM). The dynamical models are consistently represented in a pulsating–rotating frame, where an analytical approach is leveraged to provide insight on the perturbations that are present in an ephemeris model as compared to the CR3BP.

Then, capabilities and limitations of two intermediate models, the Elliptic Restricted Three-Body Problem (ER3BP) and the Bi-Circular Restricted Four-Body Problem (BCR4BP), are assessed. The nearness of the respective terms, i.e., pulsation and solar gravity, are compared between the intermediate models and the HFEM. Impact of the model parameters and the epoch initialization schemes are discussed for these models.

To confirm these insights, a sample transition process for Earth–Moon L₂ halo orbits is provided. The numerical results constructed for a wide range of epochs validate the proposed approach in assessing the transition process from the CR3BP to the HFEM for a selected set of parameters. The current work suggests a first step in a strategy to assess the dominant frequencies associated with the HFEM perturbations and apply different intermediate models under various conditions.

Acknowledgements The authors would like to thank Kenza Boudad and rest of the Multi-Body Dynamics Group members for insightful discussions. The first author would like to thank Kwanjeong Educational Foundation for the financial support. Support from NASA Johnson Space Center under cooperative Agreement Number 80NSSC18M0122 is appreciated.

Declarations

conflict of interest On behalf of all authors, the corresponding author states that there is no conflict of interest.

Appendix A: Derivations of Equation (22)

The acceleration terms in Eq. (21) are rearranged to yield cancellations and a more useful form. First, note that the familiar relative acceleration of the Moon with respect to Earth is evaluated as follows,

$$\begin{aligned}\vec{A}_{EM} &= -\frac{\tilde{\mu}_E + \tilde{\mu}_M}{R_{EM}^3} \vec{R}_{EM} + \sum_{j \in \mathcal{A}} \tilde{\mu}_j \left(\frac{1}{R_{jE}^3} \vec{R}_{jE} - \frac{1}{R_{jM}^3} \vec{R}_{jM} \right) \\ &= \frac{\tilde{\mu}_E + \tilde{\mu}_M}{l^2} \left(-\hat{x} + \sum_{j \in \mathcal{A}} \mu_j \left(\frac{1}{\rho_{jE}^3} \vec{\rho}_{jE} - \frac{1}{\rho_{jM}^3} \vec{\rho}_{jM} \right) \right).\end{aligned}\quad (1)$$

Then, for the ephemeris model, $\ddot{\vec{\rho}}_{\mathcal{A}}$ is denoted as $\ddot{\vec{\rho}}_{\mathcal{A},H}$, where each coefficient in Eq. (21) is evaluated with instantaneous ephemerides data. The \hat{x} -component of $\ddot{\vec{\rho}}_{\mathcal{A},H}$ is evaluated as, $\ddot{\vec{\rho}}_{\mathcal{A},H} \cdot \hat{x} = b_1 + (b_7 - 1)x + b_9y + b_8z - \sum_{j \in \mathcal{A}} \frac{\mu_j}{\rho_{jc}^3} (x - x_j)$. Here, note that b_1 is evaluated as,

$$b_1 = \sum_{j \in \mathcal{A}} \mu_j \left(\frac{1 - \mu}{\rho_{jE}^3} (-\mu - x_j) + \frac{\mu}{\rho_{jM}^3} (1 - \mu - x_j) \right).\quad (2)$$

Next, b_7 results in the following,

$$\begin{aligned} b_7 - 1 &= -\frac{l''}{(t')^2 l} + \frac{h^2}{(t')^2 l^4} - 1 = -\frac{l(\vec{R}_{EM} \cdot \vec{A}_{EM} + V_{EM}^2) - l'(\vec{R}_{EM} \cdot \vec{V}_{EM})}{(t')^2 l^3} \\ &\quad + \frac{l^2(V_{EM}^2 - l'^2)}{(t')^2 l^4} - 1 \\ &= -\frac{\vec{A}_{EM} \cdot \hat{x}}{(t')^2 l} - 1 = \sum_{j \in \mathcal{A}} \mu_j \left(\frac{1}{\rho_{jE}^3} (\mu + x_j) + \frac{1}{\rho_{jM}^3} (1 - \mu - x_j) \right), \end{aligned} \quad (3)$$

where leveraging $\vec{R}_{EM} = l\hat{x}$, and $h = l\sqrt{V_{EM}^2 - l'^2}$. Similarly, b_8 is evaluated as,

$$b_8 = -\frac{1}{t'^2 l} \vec{A}_{EM} \cdot \hat{z} = \sum_{j \in \mathcal{A}} \mu_j \left(\frac{1}{\rho_{jE}^3} z_j - \frac{1}{\rho_{jM}^3} z_j \right). \quad (4)$$

Finally, b_9 results in,

$$b_9 = \frac{h'}{(t')^2 l^2} = \frac{\hat{z} \cdot (\vec{R}_{EM} \times \vec{A}_{EM})}{(t')^2 l^2} = \frac{1}{t'^2 l} \vec{A}_{EM} \cdot \hat{y} = \sum_{j \in \mathcal{A}} \mu_j \left(-\frac{1}{\rho_{jE}^3} y_j + \frac{1}{\rho_{jM}^3} y_j \right). \quad (5)$$

Repeating a similar process for $\ddot{\rho}_{\mathcal{A},H} \cdot \hat{y}$ and $\ddot{\rho}_{\mathcal{A},H} \cdot \hat{z}$ results in the following expression,

$$\begin{aligned} \ddot{\rho}_{\mathcal{A},H} &= -\sum_{j \in \mathcal{A}} \mu_j \left(\frac{\ddot{\rho}_{jc}}{\rho_{jc}^3} + \frac{\ddot{\rho}_{Mc} \cdot \hat{x}}{\rho_{jE}^3} \ddot{\rho}_{jE} - \frac{\ddot{\rho}_{Ec} \cdot \hat{x}}{\rho_{jM}^3} \ddot{\rho}_{jM} - \frac{\ddot{\rho}_{Mc} \cdot \hat{y}}{\rho_{jE}^3} (\ddot{\rho}_{jE} \times \hat{z}) \right. \\ &\quad \left. + \frac{\ddot{\rho}_{Ec} \cdot \hat{y}}{\rho_{jM}^3} (\ddot{\rho}_{jM} \times \hat{z}) - \left(\frac{zz_j}{\rho_{jE}^3} - \frac{zz_j}{\rho_{jM}^3} \right) \hat{x} \right) \dots \\ &\quad + \begin{bmatrix} 0 & 0 & 0 \\ 0 & 0 & b_6 \\ 0 & -b_6 & 0 \end{bmatrix} \dot{\vec{\rho}} + \begin{bmatrix} 0 & 0 & 0 \\ 0 & b_{12} - b_{12a} & b_{11} \\ 0 & -b_{11} & b_{12} - b_{12a} \end{bmatrix} \vec{\rho}. \end{aligned} \quad (6)$$

The above equation is the same as Eq. (22), concluding the derivations.

Appendix B: Derivations of Equation (24)

Further simplification of Eq. (22) for $\ddot{\rho}_{\mathcal{A},H}$ is deduced from the additional assumptions. Assuming that $\rho_j \gg 1$, the inverse cubes of distance from j to the s/c, Earth, Moon, are linearized as,

$$\frac{1}{\rho_{jc}^3} \approx \frac{1}{\rho_j^3} + \frac{3}{\rho_j^5} (x_j x + y_j y + z_j z) \quad (7)$$

$$\frac{1}{\rho_{jE}^3} \approx \frac{1}{\rho_j^3} + \frac{3}{\rho_j^5} x_j (-\mu) \quad (8)$$

$$\frac{1}{\rho_{jM}^3} \approx \frac{1}{\rho_j^3} + \frac{3}{\rho_j^5} x_j (1 - \mu), \quad (9)$$

respectively. Utilizing these linearized functions, the expressions for the terms in Eq. (22) are reduced to simpler formulations. For the \hat{x} -direction, the resulting expression is,

$$\ddot{\rho}_{\mathcal{A},H} \cdot \hat{x} \approx \sum_{j \in \mathcal{A}} \left(\frac{3\mu_j}{\rho_j^5} \cdot 2x_j y_j y \right). \quad (10)$$

Next, the approximate accelerations for the \hat{y} and \hat{z} -directions are evaluated as,

$$\ddot{\rho}_{\mathcal{A},H} \cdot \hat{y} \approx \sum_{j \in \mathcal{A}} \frac{3\mu_j}{\rho_j^5} \left((y_j^2 - x_j^2)y + y_j z_j z \right) + (b_{12} - b_{12a})y + b_{11}z + b_6 \dot{z} \quad (11)$$

$$\ddot{\rho}_{\mathcal{A},H} \cdot \hat{z} \approx \sum_{j \in \mathcal{A}} \frac{3\mu_j}{\rho_j^5} \left(y_j z_j y + z_j z_j z \right) - b_{11}y + (b_{12} - b_{12a})z - b_6 \dot{y}, \quad (12)$$

where coefficients b_6 , b_{11} , and $b_{12} - b_{12a}$ are also well approximated. From Table 2, the expressions for these coefficients consist solely of $\vec{A}_{EM} \cdot \hat{z}$ and $\vec{J}_{EM} \cdot \hat{z}$. The first term, $\vec{A}_{EM} \cdot \hat{z}$, is linearized as,

$$\vec{A}_{EM} \cdot \hat{z} \approx t'^2 l \sum_{j \in \mathcal{A}} \frac{3\mu_j}{\rho_j^5} x_j z_j. \quad (13)$$

Leveraging this expression, the second term, $\vec{J}_{EM} \cdot \hat{z}$, is linearized as,

$$\begin{aligned} \vec{J}_{EM} \cdot \hat{z} &= (\vec{A}_{EM} \cdot \hat{z})' - \vec{A}_{EM} \cdot \hat{z}' = (\vec{A}_{EM} \cdot \hat{z})' - \frac{h'}{h} (\vec{A}_{EM} \cdot \hat{z}) \\ &\approx K_1 \sum_{j \in \mathcal{A}} \frac{3\mu_j}{\rho_j^5} x_j z_j + t'^2 l \sum_{j \in \mathcal{A}} \left(\frac{3\mu_j}{\rho_j^5} (x_j \dot{z}_j + \dot{x}_j z_j) \right. \\ &\quad \left. - \frac{15\mu_j}{\rho_j^7} x_j z_j (\dot{x}_j x_j + \dot{y}_j y_j + \dot{z}_j z_j) \right), \end{aligned} \quad (14)$$

where $K_1 = 2t't''l + t'^2 l' - \frac{h't'^2 l}{h}$. These quantities are utilized to compute b_6 , b_{11} , and $b_{12} - b_{12a}$, where it is noted that the linearized expressions contain z_j and \dot{z}_j within the summation, or, the out-of-plane position and velocity components of the additional bodies with respect to the pulsating–rotating frame. Additionally, if additional bodies are negligible except for the Sun, and assuming that $|z_S| \ll \rho_S$, or the \hat{z} -component of the solar position is negligible, the following linearized expression is produced,

$$\ddot{\rho}_{\mathcal{A},H} \approx \ddot{\rho}_{\mathcal{A},L} := \frac{3\mu_S}{\rho_S^5} (2x_S y_S y \hat{x} + (y_S^2 - x_S^2)y \hat{y}) = \frac{3\mu_S}{\rho_S^3} y (\sin 2\theta_S \hat{x} - \cos 2\theta_S \hat{y}), \quad (15)$$

concluding the derivations of Eq. (24).

References

- Acton, C., Bachman, N., Semenov, B., et al.: A look toward the future in the handling of space science mission geometry. *Planet. Space Sci.* **150**, 9–12 (2018). <https://doi.org/10.1016/j.pss.2017.02.013>
- Angelopoulos, V.: The ARTEMIS mission. *Space Sci. Rev.* **165**(1), 3–25 (2011). <https://doi.org/10.1007/s11214-010-9687-2>
- Boudad, K.K., Howell, K.C., Davis, D.C.: Analogs for earth-moon halo orbits and their evolving characteristics in higher-fidelity force models. In: AIAA SCITECH 2022 Forum, p. 1276 (2022)

- Boudad, K.K.: Trajectory design between cislunar space and sun–earth libration points in a four-body model. Ph.D. Dissertation, Purdue University, West Lafayette, Indiana (2022)
- Boudad, K.K., Howell, K.C., Davis, D.C.: Dynamics of synodic resonant near rectilinear halo orbits in the bicircular four-body problem. *Adv. Space Res.* **66**(9), 2194–2214 (2020). <https://doi.org/10.1016/j.asr.2020.07.044>
- Crusan, J.C., Smith, R.M., Craig, D.A., et al.: Deep space gateway concept: extending human presence into cislunar space. In: 2018 IEEE Aerospace Conference, pp. 1–10. IEEE (2018)
- Davis, D.C., Phillips, S.M., Howell, K.C., et al.: Stationkeeping and transfer trajectory design for spacecraft in cislunar space. In: AAS/AIAA Astrodynamics Specialist Conference, pp. 1–20 (2017)
- Dei Tos, D.A., Topputo, F.: On the advantages of exploiting the hierarchical structure of astrodynamical models. *Acta Astronautica* **136**, 236–247 (2017). <https://doi.org/10.1016/j.actaastro.2017.02.025>
- Dei Tos, D.A., Topputo, F.: Trajectory refinement of three-body orbits in the real solar system model. *Adv. Space Res.* **59**(8), 2117–2132 (2017). <https://doi.org/10.1016/j.asr.2017.01.039>
- Dei Tos, D.A.: Automated trajectory refinement of three-body orbits in the real solar system model. Master's Thesis, Politecnico di Milano, Italy (2014)
- Ferrari, F., Lavagna, M.: Periodic motion around libration points in the elliptic restricted three-body problem. *Nonlinear Dyn.* **93**(2), 453–462 (2018). <https://doi.org/10.1007/s11071-018-4203-4>
- Gómez, G., Jorba, A., Simó, C., et al.: Dynamics and Mission Design Near Libration Points: Volume III: Advanced Methods for Collinear Points. World Scientific (2001)
- Gómez, G., Masdemont, J.J., Mondelo, J.M.: Solar system models with a selected set of frequencies. *Astron. Astrophys.* **390**(2), 733–749 (2002). <https://doi.org/10.1051/0004-6361:20020625>
- Hoffman, A., Park, B., Roorda, T., et al.: Trajectory design for a secondary payload within a complex gravitational environment: the khon-1 spacecraft. In: 2022 AAS/AIAA Astrodynamics Specialist Conference (2022)
- Hou, X., Liu, L.: On quasi-periodic motions around the triangular libration points of the real earth-moon system. *Celest. Mech. Dyn. Astron.* **108**(3), 301–313 (2010). <https://doi.org/10.1007/s10569-010-9305-3>
- Jorba, A., Villanueva, J.: On the persistence of lower dimensional invariant tori under quasi-periodic perturbations. *J. Nonlinear Sci.* **7**(5), 427–473 (1997). <https://doi.org/10.1007/s00329900036>
- Jorba-Cusco, M., Farrés, A., Jorba, À.: Two periodic models for the earth-moon system. *Front. Appl. Math. Stat.* **4**(32), 1–14 (2018). <https://doi.org/10.3389/fams.2018.00032>
- Lian, Y., Gómez, G., Masdemont, J.J., et al.: A note on the dynamics around the Lagrange collinear points of the earth-moon system in a complete solar system model. *Celest. Mech. Dyn. Astron.* **115**, 185–211 (2013). <https://doi.org/10.1007/s10569-012-9459-2>
- McCarthy, B.P.: Cislunar trajectory design methodologies incorporating quasi-periodic structures with applications. Ph.D. Dissertation, Purdue University, West Lafayette, Indiana (2022)
- Ocampo, C.: An architecture for a generalized spacecraft trajectory design and optimization system. In: Libration Point Orbits and Applications, pp. 529–571 (2003). https://doi.org/10.1142/9789812704849_0023
- Oguri, K., Oshima, K., Campagnola, S., et al.: Equileus trajectory design. *J. Astronaut. Sci.* **67**(3), 950–976 (2020). <https://doi.org/10.1007/s40295-019-00206-y>
- Olikara, Z.P.: Computation of quasi-periodic tori and heteroclinic connections in astrodynamics using collocation techniques. Ph.D. Dissertation, University of Colorado at Boulder, Boulder, Colorado (2016)
- Park, B.: Low-thrust trajectory design for tours of the Martian moons. Master's Thesis, Purdue University, West Lafayette, Indiana (2021)
- Park, R.S., Folkner, W.M., Williams, J.G., et al.: The JPL planetary and lunar ephemerides DE440 and DE441. *Astron. J.* **161**(3), 105 (2021). <https://doi.org/10.3847/1538-3881/abd414>
- Peng, H., Bai, X.: Natural deep space satellite constellation in the Earth–Moon elliptic system. *Acta Astronaut.* **153**, 240–258 (2018). <https://doi.org/10.1016/j.actaastro.2018.01.008>
- Sanaga, R.R., Howell, K.: Synodic resonant halo orbits in the hill restricted four-body problem. In: 33rd AAS/AIAA Spaceflight Mechanics Meeting (2023)
- Scheuerle, S.: Construction of ballistic lunar transfers in the earth-moon-sun system. Master's Thesis, Purdue University, West Lafayette, Indiana (2021)
- Szebehely, V.: Theory of Orbit: The Restricted Problem of Three Bodies. Academic Press (1967)
- The MathWorks Inc.: MATLAB version: 9.7.0 (R2019b) (2019). <https://www.mathworks.com>
- Williams, J., Lee, D., Whitley, R., et al.: Targeting cislunar near rectilinear halo orbits for human space exploration. In: 27th AAS/AIAA Space Flight Mechanics Meeting (2017)

Springer Nature or its licensor (e.g. a society or other partner) holds exclusive rights to this article under a publishing agreement with the author(s) or other rightholder(s); author self-archiving of the accepted manuscript version of this article is solely governed by the terms of such publishing agreement and applicable law.